Journal of Archaeological Science: Reports 46 (2022) 103703

Contents lists available at ScienceDirect

Journal of Archaeological Science: Reports

journal homepage: www.elsevier.com/locate/jasrep

New approaches for the study of faience using beads from Southern Portugal

Mafalda Costa [a,b,*], Pedro Barrulas [a], Ana Margarida Arruda [c], Rui Barbosa [d], Peter Vandenabeele [b,e], José Mirão [a,f,*]

[a] HERCULES Laboratory, University of Évora, Largo Marquês de Marialva 8, 7000-809 Évora, Portugal
[b] Archaeometry Research Group, Department of Archaeology, Ghent University, Sint–Pietersnieuwstraat 35, B–9000 Ghent, Belgium
[c] UNIARQ – Archaeological Center of the University of Lisbon, Faculdade de Letras, Alameda da Universidade, 1600-214 Lisboa, Portugal
[d] Arqueohoje, Rua da Escola, Lote 9, Loja 2, Santa Eulália, 3500-682 Viseu, Portugal
[e] Raman Spectroscopy Research Group, Department of Chemistry, Ghent University, Krijgslaan 281, S12, 9000 Gent, Belgium
[f] Geosciences Department, School of Sciences and Technology, University of Évora, Colégio Luís António Verney, Rua Romão Ramalho, 59, 7000-671 Évora, Portugal

ARTICLE INFO

Keywords:
Faience
LA-ICP-MS
Mapping
Geochemistry
Phoenician-Punic
Iron Age
Provenance

ABSTRACT

A collection of 30 faience beads recovered from the Iron Age necropolis of Vinha das Caliças 4 (Beja, Portugal) was analyzed in order to identify their production technology and provide insights into their possible provenance. The multi-analytical approach employed, combining laser ablation inductively coupled plasma mass spectrometry (LA-ICP-MS), variable pressure scanning electron microscope coupled with energy dispersive X-ray spectrometry (VP-SEM-EDS) and micro-X-ray diffraction (μ-XRD), highlights the difficulties that arise from the analysis of weathered faience objects, and which are augmented by their intrinsic heterogeneous nature.

VP-SEM-EDS analysis and LA-ICP-MS mapping revealed that the disk-shaped faience beads were manufactured using the cementation glazing method. Copper, most likely in the form of bronze scrapings, was used to impart a blue-green hue to these beads. Micro-XRD also revealed that the disk-shaped beads were manufactured using feldspathic sand. On the other hand, the cubic-shaped bead, identified as an Egyptian blue frit by VP-SEM-EDS and μ-XRD, owes its vivid blue color to the tubular crystals of this well-known synthetic pigment.

Trace element analysis suggests that all beads were manufactured in the Levant region using coastal sands.

Ultimately, this study highlighted the importance of the use of a combination of microstructural and geochemical criteria in the identification of faience production technology and provenance. The importance of the selection of the sampling strategy in LA-ICP-MS analysis of weathered faience objects was also emphasized.

1. Introduction

Archaeological materials and man-made artworks are frequently studied in an attempt to determine their material history – their provenance, production date, technology, use, and the alteration or deterioration they were subjected to overtime. Studying these man-made objects allows a better understanding of the history and ethnography of the communities that produced, employed, and exchanged them. Moreover, these objects are also a testimony of the relationship between these societies and their surrounding environment, particularly with regard to the availability of raw materials.

Here, a multi-technique approach, combining laser ablation inductively coupled plasma mass spectrometry (LA-ICP-MS), variable pressure scanning electron microscope coupled with energy dispersive X-ray spectrometry (VP-SEM-EDS) and micro-X-ray diffraction (μ-XRD), was used to identify the production technology of Iron Age faience beads from Southern Portugal and provide insights into their possible provenance. The difficulties that arise from the analysis of weathered faience objects, augmented by their intrinsic heterogeneous nature, are highlighted. Moreover, this work emphasizes the importance of the use of multi-analytical approaches in the study of faience artefacts and presents the first results of the use of LA-ICP-MS to obtain elemental maps of this complex material. The importance of the selection of the sampling strategy in LA-ICP-MS analysis of weathered faience objects will also be

* Corresponding authors at: HERCULES Laboratory, University of Évora, Largo Marquês de Marialva 8, 7000-809 Évora, Portugal.
E-mail addresses: mcosta@uevora.pt (M. Costa), pbarrulas@uevora.pt (P. Barrulas), ana2@campus.ul.pt (A.M. Arruda), rbarbosa@arqueohoje.com (R. Barbosa), peter.vandenabeele@ugent.be (P. Vandenabeele), jmirao@uevora.pt (J. Mirão).

https://doi.org/10.1016/j.jasrep.2022.103703
Received 10 February 2022; Received in revised form 21 September 2022; Accepted 21 October 2022

underlined.

1.1. Faience objects

Faience, also referred to as Egyptian faience, was first manufactured in the late 5th millennium B.C. in Mesopotamia, before spreading to Egypt, where its production developed and flourished until the Roman period (Matin and Matin, 2012; Nobel, 1969; Tite and Shortland, 2008). Faience production technology rapidly disseminated throughout Europe, leading to its manufacture in a large region, including most of central and southern Europe, Russia, and Britain (Angelini et al., 2004; Matin and Matin, 2012; Purowski, 2020; A. Shortland et al., 2007a; Tite and Shortland, 2008). Faience was also produced in western and southern Asia, in the Indus Valley from the 3rd millennium B.C. to the early 2nd millennium B.C. (Gu et al., 2016; Matin and Matin, 2012; Tite and Shortland, 2008), and in China, where it appeared in the late 2nd millennium B.C. (Gu et al., 2014). In the Near East, particularly in Iran, faience is still being produced using traditional techniques (Matin and Matin, 2012).

Faience generally consists of a sand or finely ground quartz core coated with a colored alkaline-lime-silicate glaze (Matin and Matin, 2012; Rehren, 2008; Tite et al., 2007, 1983; Tite and Shortland, 2008; Toffolo et al., 2013). Three different glazing methods can be employed in the production of faience objects – application glazing, efflorescence glazing or cementation glazing (or Qom technique) (Matin and Matin, 2012; Tite et al., 1983; Toffolo et al., 2013). Efflorescence glazing is best suited for the manufacture of large objects, while application glazing was primarily used in the production of medium-sized objects, including tiles, and cementation glazing was employed to mass-produce small objects such as beads and rings (Matin and Matin, 2012; Tite et al., 2007). Macroscopic evidence, such as the presence or absence of brush marks, drips and running lines and stand marks have been used in the identification of faience glazing methods (Matin and Matin, 2012).

Regardless of the glazing technique employed, microstructural characterization of faience objects has generally revealed a triple-layered structure: 1) a quartz-rich core, also referred to as body, in which the grains are held in place by variable amounts of interparticle glass; 2) a buffer or interaction layer, in which the grains are embedded in an almost continuous glass matrix; and 3) an external quartz-free glaze (Matin and Matin, 2012; Tite et al., 1983). This triple-layered structure can be absent when the objects are weathered (A. Shortland et al., 2007a). Moreover, when the crystalline grains are embedded in the vitreous phase, causing the structure to appear uniform without defined layers, the material is classified as glassy faience (Purowski, 2020; Santopadre and Verità, 2000).

Tite et al. (1983) and Tite & Bimson (1986) proposed that the different glazing methods could be distinguished based on microstructural criteria, including the thickness of the glaze and interaction layers, the boundary between the interaction layer and the core, and the amount of interparticle glass present in the core (Tite et al., 1983; Tite and Bimson, 1986). Vandiver (1998), on the other hand, demonstrated that the addition of glazing mixture to the core, which is known to facilitate molding the object into the desired shape, could result in changes in the amount of interparticle glass present in the core and alter the nature of the interaction layer-core boundary (Vandiver, 1998). Moreover, changes in firing temperature and time, which may increase the thickness of the interaction layer, can lead to the incorrect identification of the glazing method employed in the manufacture of faience artifacts (Vandiver, 1998). In fact, faience replication experimental studies have frequently recommended caution when glazing method identification is conducted solely using macroscopic and microstructural criteria (Matin and Matin, 2012; Vandiver, 1998). The work by Tite et al. (2007) suggests that compositional profiles may also be used to distinguish between faience glazing methods (Tite et al., 2007).

2. Materials & methods

2.1. Materials

Thirty faience beads were selected from within the bead assemblage found in Vinha das Caliças 4 (Beja, Portugal), a 6th century BCE Iron Age necropolis (Arruda et al., 2016). This indigenous necropolis was excavated in 2008 and 2009 enabling the recovery of a wide range of exotic materials attributed to the Phoenician-Punic civilization including glass beads and faience beads and scarabs (Arruda et al., 2016; Costa et al., 2021, 2019a, 2019b).

Three hundred and nine annular or disk-shaped faience beads were found in two different graves; 18 beads were recovered from a rich female grave (burial 48), which contained, among other finds, glass beads, as well as the previously studied scarabs (Costa et al., 2019a), while the majority (291) were found in grave (burial 41) where no osteological remains were present. Various fragments of these faience beads were also found in both graves. Twenty-nine disk-shaped beads (ca. 4–5 mm diameter, ca. 1 mm thickness and an aperture diameter of ca. 2 mm), with hues varying from light green to blue-green (Fig. 1a and Figure S1 – Supplementary information) were randomly selected from the assemblage found in burial 41 to be included in this study. A vivid blue cubic-shaped bead (sample C1; ca. 5 × 5 × 5 mm) recovered from a female grave (burial 47) was also included in this study (Fig. 1b and Figure S1 – Supplementary information). Four disk-shaped beads were selected, embedded in epoxy resin and polished for further analysis (samples CS1 to CS4). The remaining 25 disk-shaped faience beads, as well as the cubic bead (the only one of its kind found in Vinha das Caliças 4), were not subjected to any kind of sample preparation prior to their analysis.

2.2. Methods

A Hitachi™ S3700N SEM coupled to a QUANTAX EDS microanalysis system equipped with a Bruker™ XFlash 5010 SDD EDS Detector® and a Bruker™ D8 Discover® in micro-X-ray diffraction configuration (μ-XRD) were used to analyze all thirty samples. All samples were analyzed by VP-SEM-EDS at 40 Pa (low vacuum), with an accelerating voltage of 20 kV and a working distance of ca. 10 mm. The Esprit1.9 (Bruker™) software enabled standardless quantification (Costa et al., 2019a). Micro-XRD analyses were performed on the surface of all samples using a 2 angular range between 3 and 75°, a 0.05° step increment and measuring time of 1 s/step (Costa et al., 2019a). Phase identification was performed using the DIFFRAC.SUITE EVA® software and the ICDD PDF-2 database.

LA-ICP-MS analysis was performed using a CETAC LSX-213 G2 + laser ablation system coupled to an Agilent™ 8800 Triple Quad ICP-MS. Instrument calibration and tune optimizations followed previous studies (Costa et al., 2021, 2020, 2019c). The analytical conditions used for each measurement can be found in Table 1. The samples were analyzed in three or four distinct locations when spot analysis or line scans were performed. The first 2 or 3 s of ablation were discarded in spot analysis to eliminate possible surface contamination and weathering. Pre-ablation was performed before each line scan: a 100 μm spot size with a 50 μm/s scan rate, a frequency of 20 Hz and 100 % laser output energy was used in the analysis of the disk-shaped beads, while a 150 μm spot size with a 400 μm/s scan rate, a frequency of 20 Hz and 100 % laser output energy was used in the analysis of the cubic-shaped bead. The latter, as well as the analysis conditions used, were optimized to ensure minimal visible damage to the cubic-shaped bead.

Elemental concentrations were determined using the sum normalization calibration approach (van Elteren et al., 2009). Data reduction was performed using the GLITTER® software (version 4.4.2). Accuracy and precision for the spot analysis and line scans calculated (D'Oriano et al., 2008) using the certified reference values of SRM NIST 610 (Pearce et al., 1997) can be found in Tables S1 to S3 (Supplementary information).

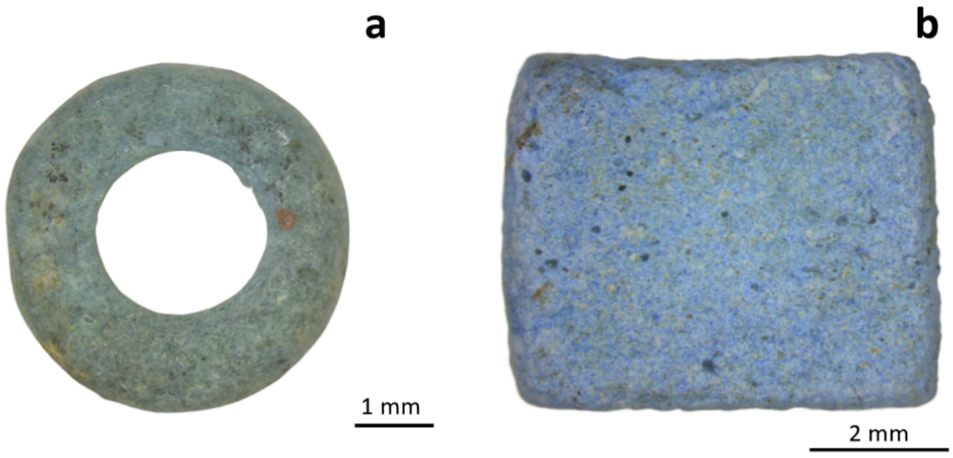

Fig. 1. Stereomicroscopy imagens of a) a blue-green disk-shaped bead; and b) of the vivid blue cubic-shaped bead. (For interpretation of the references to color in this figure legend, the reader is referred to the web version of this article.)

Table 1
Acquisition conditions, isotopes analyzed by LA-ICP-MS along with their respective dwell times. The underlined chemical elements were analyzed in the multi-line scan mode, while all elements, with the exception of phosphorous, were analyzed in the spot analysis and line scan modes.

Agilent™ 8800 Triple Quad ICP-MS			
Acquisition Mode	TRA (Time Resolved Analysis)		
Scan Type	Single Quad		
Plasma Parameters			
RF Power	1200 W		
RF Matching	1.4 V		
Sample Depth	4 mm		
Carrier Gas (Ar)	1.01 L/min		
Plasma Gas (Ar)	15 L/min		
Collision/Reaction Cell Mode	No gas		
Dwell time (ms)			
2	^{28}Si; ^{44}Ca		
5	^{27}Al; ^{43}Ca; ^{56}Fe		
10	^{23}Na; ^{24}Mg; ^{39}K; ^{45}Sc; ^{47}Ti; ^{51}V; ^{52}Cr; ^{55}Mn; ^{57}Fe; ^{59}Co; ^{60}Ni; ^{63}Cu; ^{66}Zn; ^{85}Rb; ^{88}Sr; ^{133}Cs; ^{137}Ba; ^{208}Pb		
20	^{31}P; ^{75}As; ^{89}Y; ^{90}Zr; ^{93}Nb; ^{118}Sn; ^{121}Sb; ^{139}La; ^{140}Ce; ^{141}Pr; ^{146}Nd; ^{147}Sm; ^{153}Eu; ^{157}Gd; ^{159}Tb; ^{163}Dy; ^{165}Ho; ^{166}Er; ^{169}Tm; ^{172}Yb; ^{175}Lu; ^{178}Hf; ^{181}Ta; ^{209}Bi; ^{232}Th; ^{238}U		
Laser Ablation System - CETAC LSX-213 G2+			
Analysis Mode	Spot Analysis	Line scan	Multi-line scan
Laser Energy Output (%)	100	100	10
Fluence (J/cm^2)	ca. 4	ca. 4–5	ca. 4
Spot Size (μm)	50	50 (disk-shaped beads) 100 (cubic-shaped bead)	50
Repetition Rate (Hz)	20	20 (disk-shaped beads)	20
Scan rate (μm/s)	-	10 (cubic-shaped bead)	50
Burst Count	600	10 (disk-shaped beads)	-
Space between lines (μm)	-	100 (cubic-shaped bead)	20
He carrier flow (L/min)	1	-	1
		-	
		1	

In the multi-line scan mode, the number of lines was selected in order to obtain elemental images of the entire cross-section of the disk-shaped faience beads analyzed. The multi-line scan intensities (counts per second) were converted into elemental images using the iQuant2® software, developed by the Institute of Technology of Tokyo and the University of Kyoto.

3. Results & discussion

3.1. Microstructural characterization

The VP-SEM examination of the 25 disk-shaped faience beads that were not subjected to any type of sample preparation showed clear signs of weathering, causing the frequent absence of the glaze, and consequently, the total or partial exposure of the interaction layer (Fig. 2a and 2b). In the interaction layer, angular and sub-angular sand grains are surrounded by interparticle glass (Fig. 2). However, the glaze, when present, generally displays a network of cracks running in all directions of the surface, and, in some instances, a sugar-like appearance on a microscopic level, both of which are evidence of significant weathering (Fig. 2b and 2c). Under burial conditions, glasses and glazes can undergo two different alteration processes – selective leaching and uniform dissolution. In the first, water reacts with the glass, removing alkali elements, such as sodium and potassium, producing a dealkalized, silica-rich layer; in the second, complete dissolution of all the silicate network occurs (Costa et al., 2021, 2019a,2019b; Robinet and Eremin, 2012). Selective leaching leads to the formation of silica-rich gel-like layer and promotes further glass alteration (Robinet and Eremin, 2012).

On the other hand, the VP-SEM examination of the cross-sections of four disk-shaped faience beads embedded in epoxy resin revealed triple-layered structures (Fig. 3). In these beads, the glaze layer is thin, irregular, and occasionally absent, suggesting that they are representative of the 25 faience beads that were not subjected to any type of sample preparation. It is important to note that the thinness and irregularity of the glaze layer may be used as a microstructural criterion to define the glazing method employed in the production of the beads, but it can also be the result of weathering.

The interaction layer of the disk-shaped faience beads never exceeds 350 μm and is demarked from the core layer by an uneven but clearly defined boundary. The sand grains visible in both the core and interaction layer are generally angular and sub-angular, respectively, and have variable size, with larger grains exceeding 100 μm in diameter.

Little or no interparticle glass appears to be present in the core in any of the disk-shaped beads. However, in sample CS4, the sand grains of the core are occasionally surrounded by a calcium phosphate phase, with significant fluorine amounts (Fig. 4a and 4b). Given its seemingly

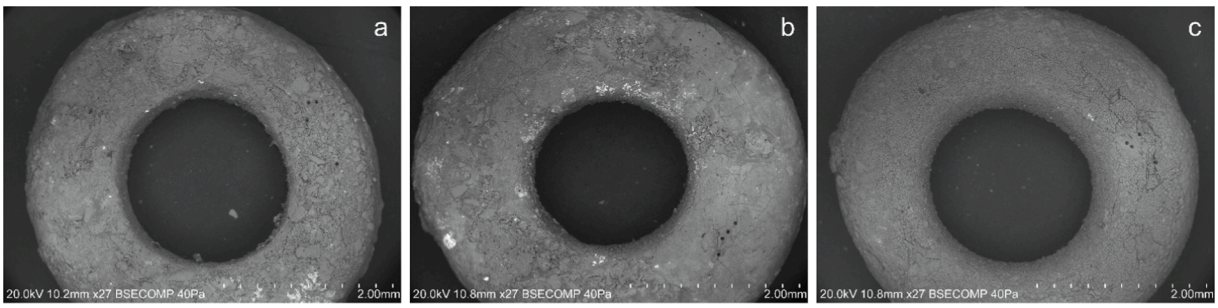

Fig. 2. Representative VP-SEM images of the 25 disk-shaped faience beads that were not subjected to any type of sample preparation displaying varying degrees of weathering. a) sample 1; b) sample 12; c) sample 20.

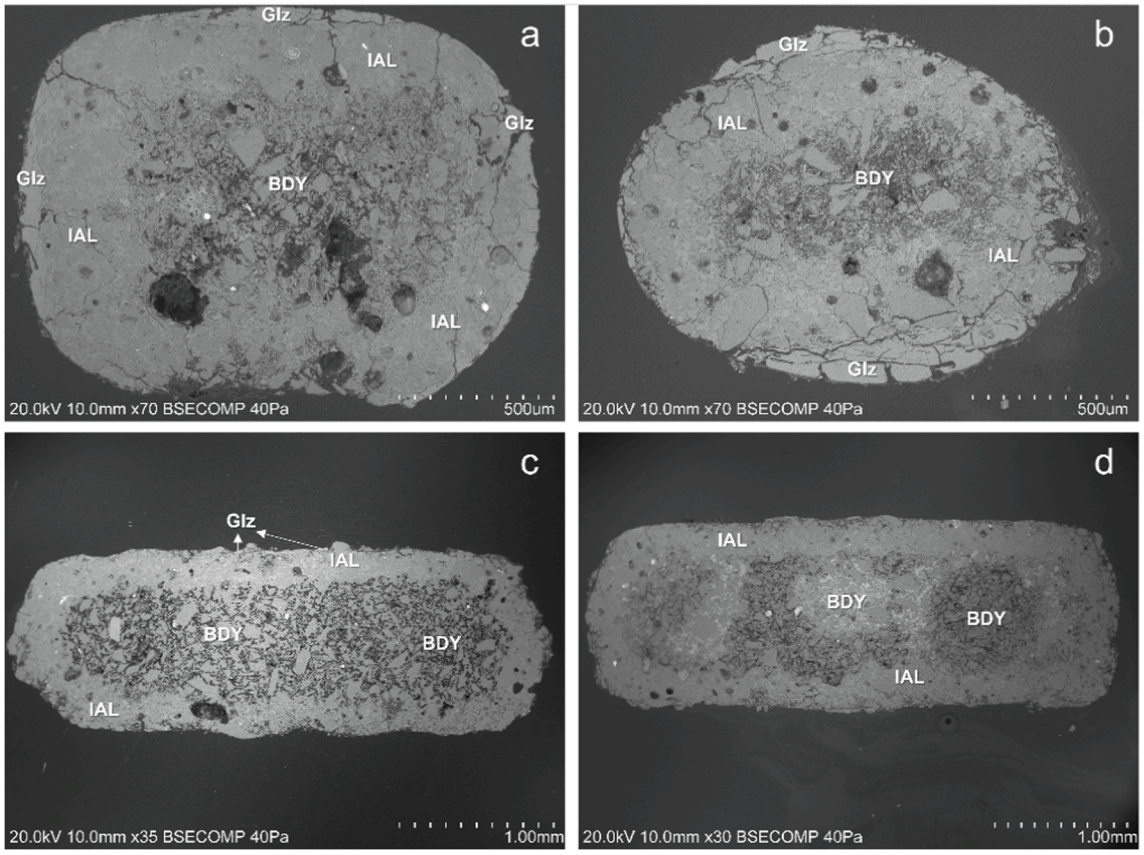

Fig. 3. VP-SEM images of each disk-shaped faience bead embedded in epoxy resin. a) CS1; b) CS2; c) CS3; d) CS4 (Abbreviations: GLZ = glaze; IAL = interaction layer; BDY = core).

localized presence within the bead's core (whitish light grey in Fig. 3d), and the increased porosity due to limited or absent interparticle glass, secondary precipitation of calcium phosphate phases cannot be excluded.

Calcium-rich deposits, most likely calcite, can also be found filling pores (Fig. 5a) and on the surface of the disk-shaped faience beads (Fig. 5b). These are most likely the result of secondary phase precipitation in the burial context, which is known to happen in calcareous soils as the ones in Vinha das Caliças 4.

Overall, the microstructural characteristics – thin and irregular glaze, thick interaction layer with a clearly defined interaction layer-core boundary and little or no interparticle glass in the core (Tite et al., 2007, 1983; Tite and Bimson, 1986; Tite and Shortland, 2008) – indicate that the cementation method was employed in the production of all the disk-shaped faience beads analyzed.

Sample C1, a cubic-shaped bead, was not embedded in epoxy due to its unique nature. However, observations of the surface of the bead, using VP-SEM, revealed a granular texture, with clusters of elongated, tabular crystals enriched in Ca, Si and Cu (which are likely Egyptian blue – $CaCuSi_4O_{10}$), surrounded by sub-angular sand grains (Fig. 6), a microstructure that suggests the bead consists of an Egyptian blue frit (Hatton et al., 2008; Toffolo et al., 2013). Calcium phosphate crystals enriched in F were also identified in sample C1 (Fig. 4c and 4d).

3.2. Mineralogical characterization

Micro-X-ray diffraction was performed on all faience beads. The disk-shaped beads were found to be composed almost exclusively of quartz. Potassium feldspar, plagioclases and calcite were also identified by μ-XRD in several beads (e.g., Fig. 7). Plagioclases, specifically albite, oligoclase and labradorite, were also identified by VP-SEM-EDS in the core and in the interaction layer in several disk-shaped beads (Figure S2

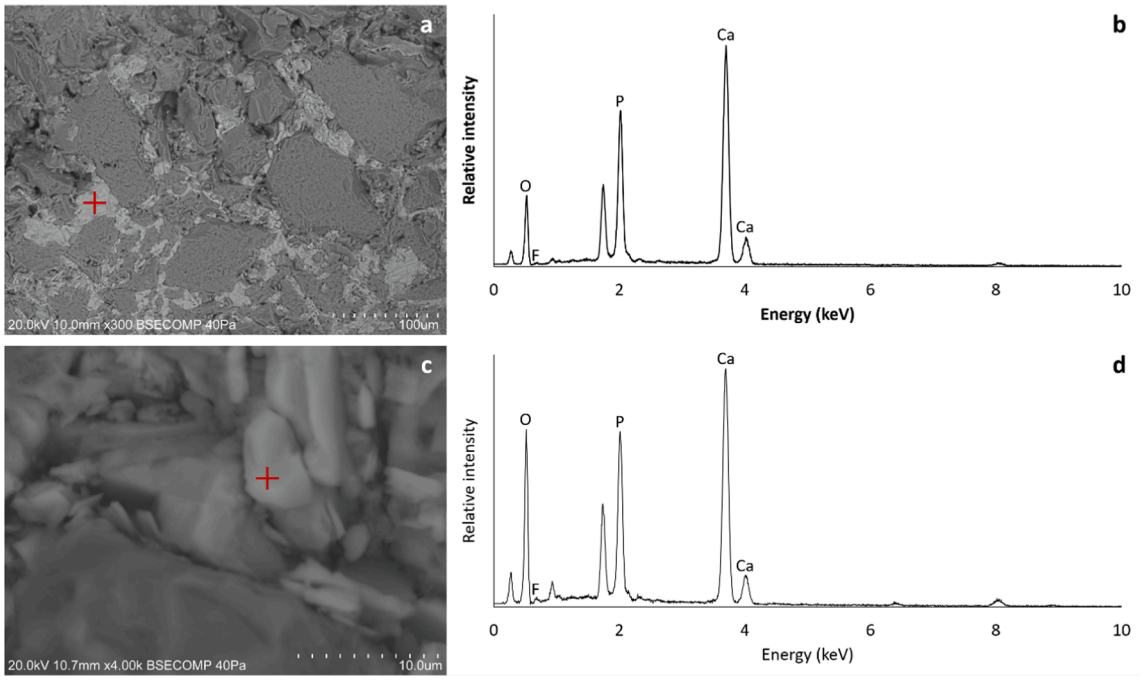

Fig. 4. VP-SEM image and respective point analysis of calcium phosphates found in sample CS4 (a and b) and sample C1 (c and d).

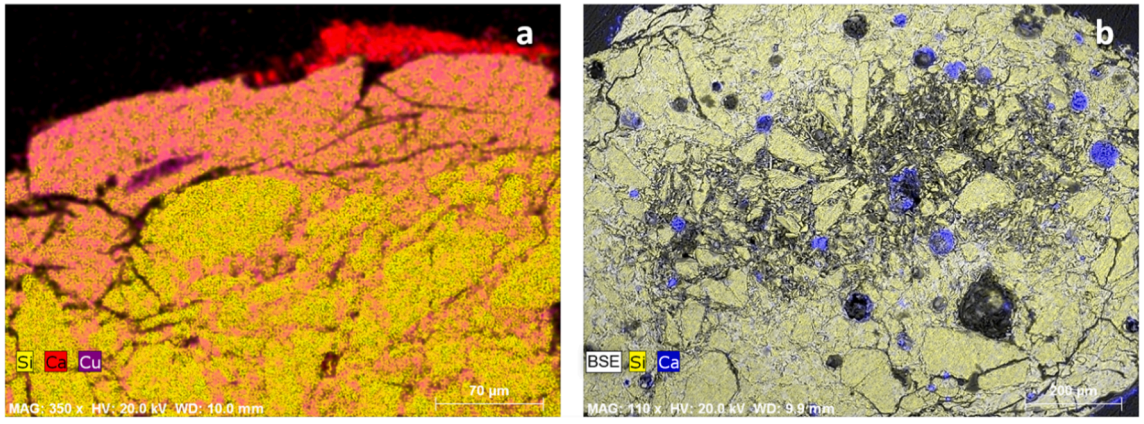

Fig. 5. Elemental mapping obtained by VP-SEM-EDS revealing the presence of calcium-rich secondary deposits filling pores and on the surface of sample CS3. (For interpretation of the references to color in this figure legend, the reader is referred to the web version of this article.)

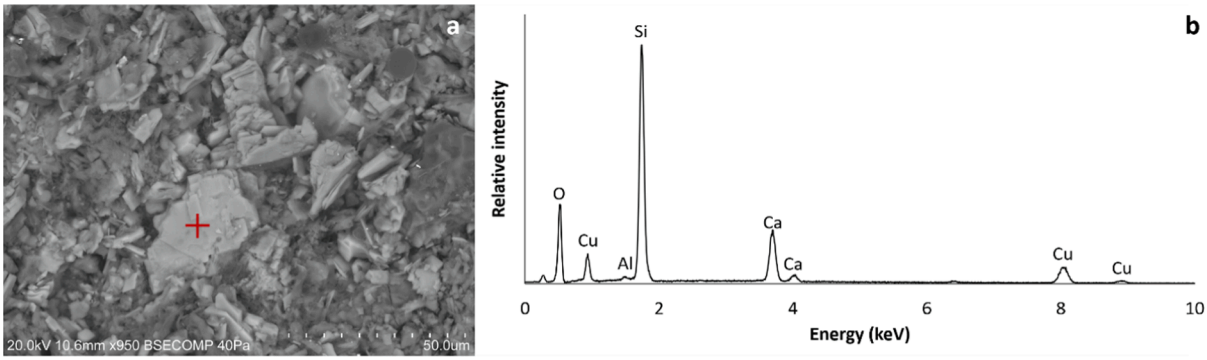

Fig. 6. VP-SEM image (a) and point analysis (b) of the tabular crystals present in sample C1 and identified as Egyptian blue.

– Supplementary information). As previously mentioned, the presence of calcite is most likely the result of secondary phase precipitation under burial conditions.

Micro-X-ray diffraction of sample C1 confirmed that it owes its color to cuprorivaite (Fig. 7), also known as Egyptian blue, a synthetic blue pigment first used at the end of the 1st Dynasty of the Old Kingdom (ca.

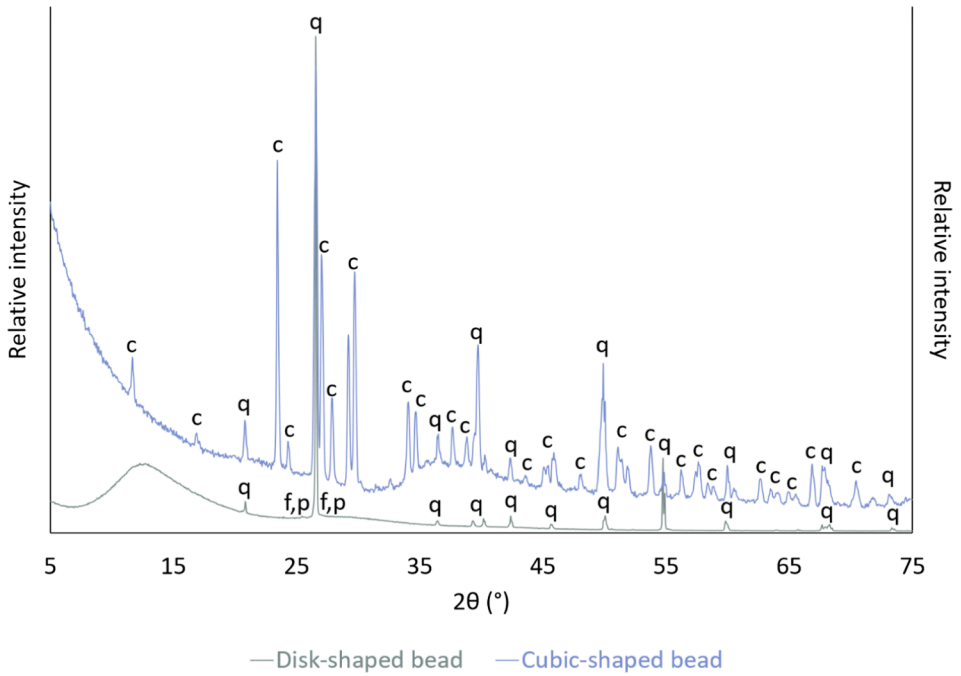

Fig. 7. X-ray diffraction patterns of a disk-shaped bead and of the cubic-shaped bead (Abbreviations: c = cuprorivaite; f = K-feldspar; p = plagioclase; q = quartz).

2900BCE) (Hatton et al., 2008). The use of the Egyptian blue pigment became widespread in the 4th Dynasty (ca. 2600–2480BCE) (Hatton et al., 2008), and it was continuously employed in the production of artworks in Egypt, Mesopotamia and Greece up to the end of the Roman period, and in Italy and central Europe until the Middle Ages (Riederer, 1997). No written records of production and commercialization of the Egyptian blue pigment have been found in Ancient Egyptian contexts (Riederer, 1997). However, Theophrastus (371–287BCE), in his book *De lapidibus* mentions the trade of a synthetic blue pigment originating in Egypt, which suggests Egyptian blue was produced in Egypt up until the 3rd century BCE and brought to Europe through commercial trade routes in place during that period (Riederer, 1997). The manufacture of Egyptian blue is described by Vitruvius in the early 1st century BCE (Hatton et al., 2008; Riederer, 1997), indicating in may have been produced outside Egypt, in modern Pozzuoli (Italy), during the Roman period. Archaeological finds from Cuma, near Pozzuoli, suggest that Egyptian blue was produced in the region during the Roman period (Grifa et al., 2016). Quartz was also identified in sample C1 by μ-XRD.

3.3. Chemical characterization

The chemical composition of the glaze and interaction layer glass of the four cross-sections of the disk-shaped faience beads analyzed by VP-SEM-EDS can be found in Table 2. The absence of sodium and potassium in almost all samples precluded the undisputed identification of the fluxing agent used in the manufacture of these faience beads. However, the low MgO values, combined with the significant Cl concentrations, could indicate that natron, a raw material deriving from evaporitic lake deposits and known to have been used in the manufacture of man-made vitreous materials since the early 4th millennium B.C. (Shortland et al., 2006), was used in their production. The chronology attributed to the necropolis of Vinha das Caliças 4, and the known gradual increase in natron glass production around the 10th to 8th century BCE is an argument in favor of the use of natron in the production of these artifacts (Conte et al., 2018; Costa et al., 2021). These results also revealed that the disk-shaped faience beads suffered selective leaching, causing the loss of the alkali elements present in the glaze and interaction layer glass.

Twenty-five disk-shaped faience beads (samples 1 to 25) were analyzed by LA-ICP-MS without any sample preparation in an attempt to determine the fluxing agent used in the manufacture of the glaze of these artifacts. In areas where the glaze was deemed to be present, four ablations spots were performed in each sample. Spot analysis in the study of faience beads was previously applied by Purowski et al. (2019). However, in this study, the absence of a deeply colored glaze, with the beads frequently displaying only a faint blue-green tint, combined with the variable thickness and occasional complete absence of the glaze, greatly hindered the selection of appropriate locations for spot analysis.

Table 2
VP-SEM-EDS results (oxides wt.%) of the four disk-shaped faience beads embedded in epoxy resin. (Abbreviation: n.d. = not detected)

	CS1		**CS2**		**CS3**		**CS4**	
	Glaze	Interaction layer glass	Glaze	Interaction layer glass	Glaze	Interaction layer glass	Glaze	Interaction layer glass
Na_2O	n.d.	n.d.	n.d.	n.d.	n.d.	n.d.	n.d.	n.d.
MgO	n.d.	0.7	n.d.	0.8	n.d.	n.d.	n.d.	0.6
Al_2O_3	0.8	1.4	n.d.	1.8	1.0	1.1	n.d.	1.4
SiO_2	83.6	83.1	84.2	85.4	87.3	87.1	86.6	84.1
Cl	1.2	1.0	2.1	n.d.	1.9	0.4	1.3	0.5
K_2O	n.d.	0.6	n.d.	n.d.	n.d.	n.d.	n.d.	n.d.
CaO	1.6	1.9	2.0	2.1	0.9	1.0	0.9	1.4
MnO	0.6	1.1	n.d.	1.3	0.7	1.2	n.d.	1.5
FeO	0.8	1.2	2.3	3.4	0.5	1.5	n.d.	2.4
CuO	11.3	9.2	9.5	5.3	7.8	7.7	11.3	8.2

As seen in Table S4 (Supplementary information), repeatability was not achieved due to the heterogeneous nature of the samples and the spots selected resulted in measurements of glaze, interaction layer sand grains, interaction layer glass or combinations of all three, as becomes apparent when observing the samples under VP-SEM after the analysis by LA-ICP-MS (Figure S3 – Supplementary information). The results obtained clearly underscore the importance of the selection of the sampling strategy used in LA-ICP-MS analysis and suggest that spot analysis should never be used in the study of weathered faience while simultaneously raising an important issue regarding the use of minimally invasive analyses to determine the provenance of these objects.

As seen in Table 2, significant amounts of copper (CuO values between 5.3 and 11.3 wt%) were detected in the glaze and interaction layer glass of the cross-sections of the disk-shaped faience beads analyzed by VP-SEM-EDS. Copper is among the first two colorants used in the production of faience, imparting blue-green or turquoise hues to the glaze (Shortland, 2002; Tite et al., 2007). Moreover, the decrease in copper content from the glaze to the core, as evidenced by Table 2, can indicate the use of the cementation glazing technique in the manufacture of these faience beads (Tite et al., 2007).

On the other hand, the detection of significant amounts of manganese and iron in the glaze and interaction layer glass (Table 2) is likely the result of the use of quartz-rich sand instead of the alternative crushed quartz pebbles. The aforementioned presence of feldspars, along with the identification of rounded or sub-rounded Fe-rich and Fe-Mn-rich crystals (e.g., Fig. 8) in the interaction and core layers of the disk-shaped faience beads supports the use of quartz-rich sand in the manufacture of these artifacts. However, the detection of significant amounts of Fe and Mn in the glaze and interaction layer glass (Table 2) may also result from the deliberate addition of these elements to produce greenish turquoise hues (iron) or darker colors (manganese) (Tite et al., 2009).

Tin-rich crystals were found by VP-SEM-EDS in cross-sections CS1 and CS3, in most disk-shaped faience beads that were not embedded in epoxy resin, and in sample C1 (Fig. 9). The presence of tin in copper-colored glass and faience has often been linked to the use of bronze scrapings (e.g. Costa et al., 2019a; Shortland et al., 2006; Smirniou and Rehren, 2013; Tite and Shortland, 2008). Tin particles with irregular shape have previously been interpreted as possible remnants of the use of tin bronze scrapings used as the copper source (Angelini et al., 2004). Therefore, the occurrence of polycrystalline tin-rich aggregates (Fig. 9a and 9b), dispersed throughout the glassy phase, suggests that tin was introduced via the copper source in the disk-shaped faience beads. However, the presence of sub-rounded tin-rich crystals in sample C1 (Fig. 9c and 9d) may indicate that cassiterite-rich placer sands were used in the production of this Egyptian blue frit or the Egyptian blue pigment. In nature, tin generally occurs as cassiterite (SnO_2) and is commonly associated with pegmatitic or granitic type rocks or placers deposits that arise from their weathering (Graf, 2000). In fact, cassiterite is among the most common heavy minerals found in several placer deposits along the Egyptian coast (e.g. Abdel-Karim and El-Shafey, 2012; Ragab et al., 2017).

Grains enriched in iron and cobalt, accompanied by Ti, Mn, Ni and Zn were also found in samples CS3 and CS4 (e.g., Fig. 10). These grains are embedded within the interaction layer glass, and present diffuse reaction rims, suggesting that they were added, probably unintentionally, as impurities within the sand source. Transition metals such as Ti, Cr, Mn, Co, Ni and Zn can be adsorbed or incorporated into the structure of iron oxides such as magnetite (Bliem et al., 2015; Costa et al., 2006; Musić and Ristic, 1992; Zhong et al., 2013).

VP-SEM-EDS analysis of the 25 disk-shaped faience beads not embedded in epoxy resin also revealed crystalline aggregates enriched in lead and vanadium (Fig. 11). Lead-vanadium crystals were previously detected in faience found in Sidon (Lebanon) (Griffiths, 2006), and in two of the scarabs found in Vinha das Caliças 4 (Costa et al., 2019a), which may indicate a common origin of all these artifacts.

Elemental mapping was performed by LA-ICP-MS on samples CS1, CS3 and CS4. These maps revealed a decrease of copper content from the glaze to the core of the beads (Fig. 12), which, as shown by Tite et al. (2007), confirms the use of the cementation glazing technique in their manufacture (Tite et al., 2007). The more diffuse boundary between the interaction layer and core, visible in the elemental map of sample CS1, may indicate that a slightly different firing regime was employed in its manufacture, causing an increase in interparticle glass in the core, or the existence of a thicker interaction layer as suggested by Vandiver (1998). Conversely, tin, which is not incorporated into the glass structure, but, as previously mentioned, appears as cassiterite aggregates dispersed throughout the glassy phase, is most abundant within the interaction and core layers (Fig. 12). This phenomenon might be explained by the poor solubility of tin oxide when compared to copper oxide (Paynter and Jackson, 2022), which causes the copper to be more easily incorporated into the glassy phase.

The elemental maps also showed that Fe, Cr and Ti are present primarily in the core, while Mn, Co, Ni, Zn and As are preferentially incorporated in the glassy phases of the glaze and interaction layers (Figures S4, S5 and S6 – Supplementary information). As aforementioned, these elements, with the exception of arsenic, are most likely introduced as impurities within the sand source. Arsenic may have been introduced via the copper source, as this metal has been found along with lead and antimony in many bronze artifacts in the Mediterranean region (e.g. Ingo et al., 2006). In fact, both lead and antimony are also present in the disk-shaped faience beads, with Sb being restricted to the core and Pb in both the interaction and core layers (Figures S4, S5 and S6 – Supplementary information). Rare earth elements (REE) and Zr also appear to be dispersed throughout the interaction layer and core (Figures S4, S5 and S6 – Supplementary information), most likely in the form of REE phosphates monazite or xenotime and zircon, respectively, which once again indicates that quartz-rich sand was used in the

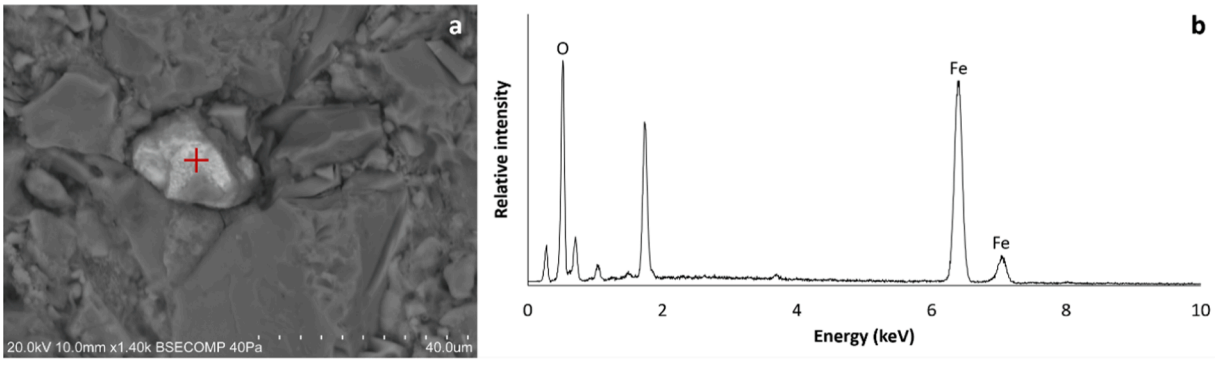

Fig. 8. VP-SEM image (a) and point analysis (b) of a sub-angular grain found in the interaction layer of sample CS1. This grain is most likely an iron oxide present as an impurity within the sand source.

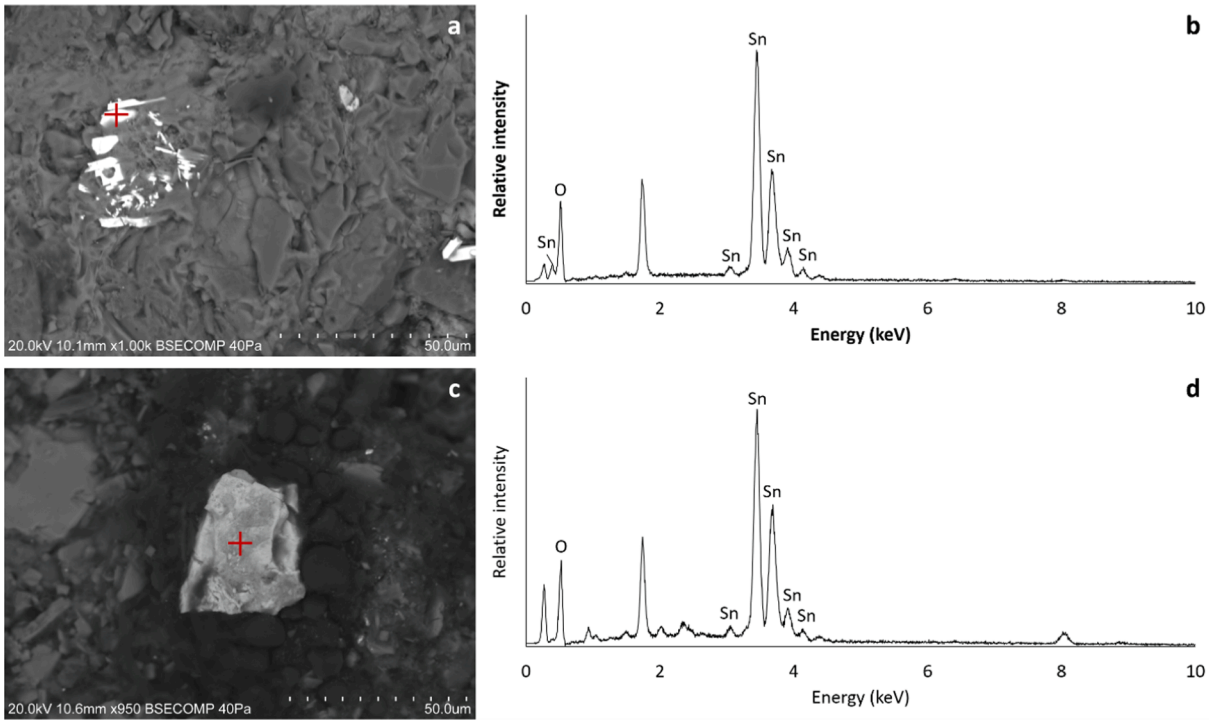

Fig. 9. VP-SEM image and respective point analysis of cassiterite found in sample CS4 (a and b) and sample C1 (c and d).

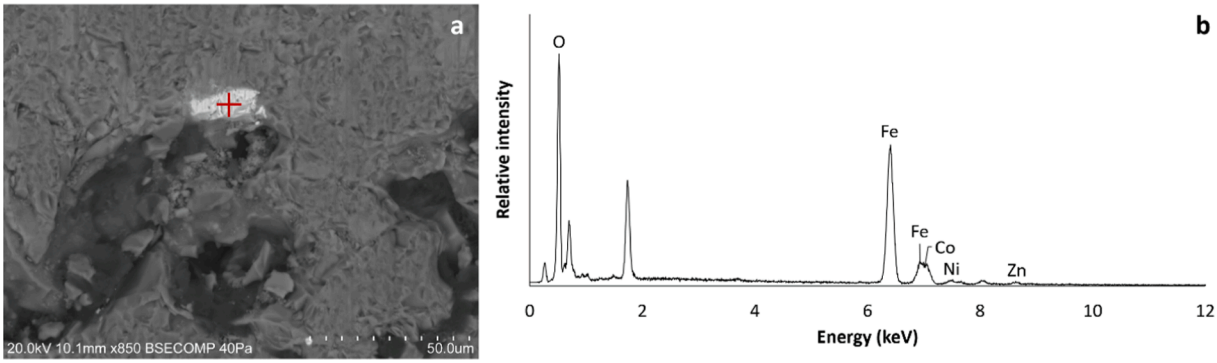

Fig. 10. a) VP-SEM image of an angular grain embedded within the interaction layer glass and presenting a diffuse reaction rim; b) point analysis of the same grain, revealing it is enriched in Fe, Co, Ni and Zn. Co, Ni and Zn are among the transition elements that can be adsorbed or incorporated into the structure of iron oxides, minerals that are commonly present in sands used for the production of vitreous artifacts.

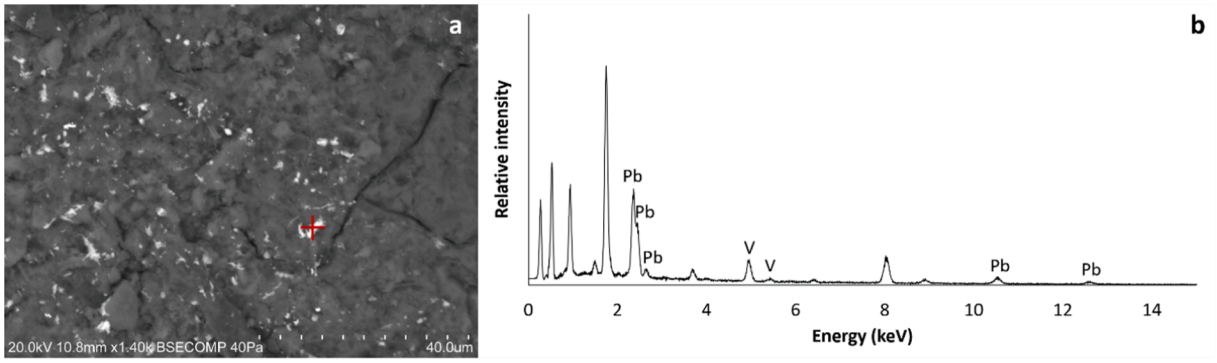

Fig. 11. VP-SEM image (a) and point analysis (b) of crystalline aggregates enriched in lead and vanadium embedded within the glassy layer of several disk-shaped faience beads which were not subjected to any type of sample preparation prior to their analysis.

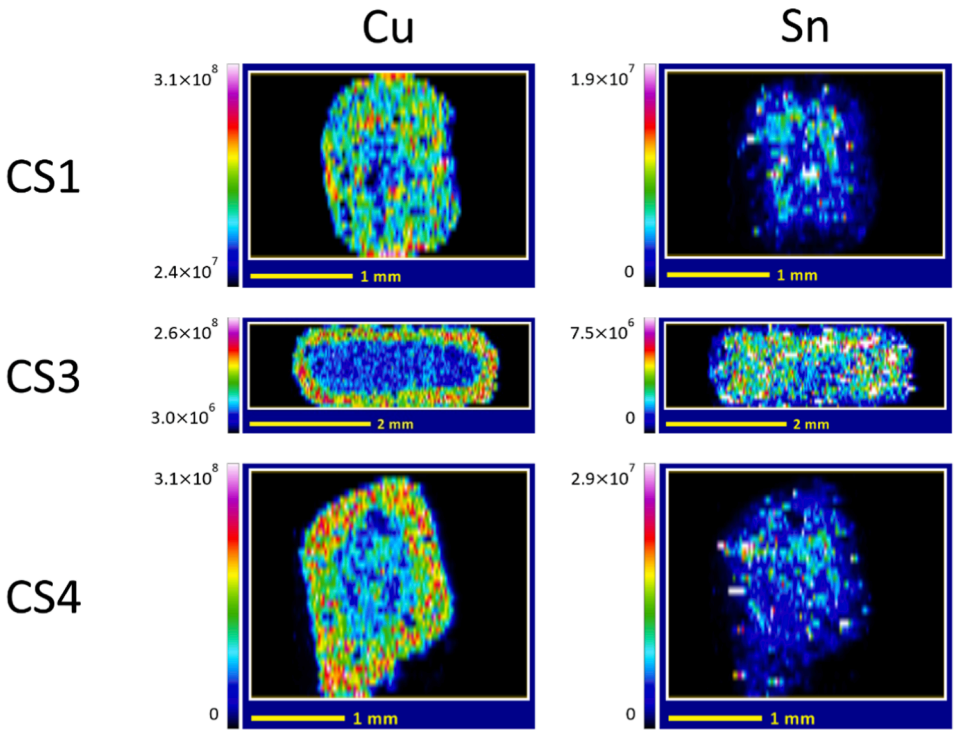

Fig. 12. Elemental mapping obtained by LA-ICP-MS of samples CS1, CS3 and CS4. The copper content decreases from the glaze to the core of the beads, in accordance with the use of the cementation glazing technique. Tin, on the other hand, seems to be dispersed throughout the glassy phase present in the interaction and core layers.

manufacture of the disk-shaped faience beads.

3.3.1. Insights into the provenance of the beads

The cross-sections of the four disk-shaped faience beads embedded in epoxy resin were also analyzed by LA-ICP-MS in order to obtain a "pseudo-bulk" composition. Given the heterogeneous nature of the materials and the previous failed attempt at reproducible results using the spot analysis sampling strategy, three replicate line scans perpendicular to the surface of the bead, and covering its entire width, were performed on each sample. Line scans were previously used by Mangone et al. (2011) in the study of faience objects from Pompeii. While this approach is not spatially resolved and, as such, does not take into account the multi-layered structure of faience objects, it provides information regarding trace elements, which could not easily be achieved given the size of these objects (ca. 5 mm in diameter), and that is essential in provenance studies. Line scan analysis was also performed on sample C1 in order to compare this Egyptian blue frit bead to the disk-shaped faience beads of Vinha das Caliças 4. The LA-ICP-MS line scan results can be found in Table 3.

Glass provenance studies rely on the principle that this material inherits the chemical fingerprint of the ingredients used in its manufacture. Unlike other ingredients used in glass production, sand is not known to have been subjected to long-distance trade (Leslie et al., 2006); primary or glass producing workshops are thought to be located near favored sand sources and, as such, distinguishing between different sources can be used to pinpoint a glass' provenance. Given the similarities between faience and glass production, the identification of the silica source used can also shed light on the geographical origin of faience objects.

Trace element analysis has commonly been used in glass provenance studies to distinguish between different sand sources (e.g. Conte et al., 2018; Costa et al., 2021, 2020,2019c; Dussubieux et al., 2009; Freestone et al., 2002; Hellemans et al., 2019; Oikonomou et al., 2018; Saitowitz, 1996; A. J. Shortland et al., 2007a; Truffa Giachet et al., 2019; Van Strydonck et al., 2018; Wedepohl et al., 2011). While sands used in glass production are composed primarily of quartz, they contain minor amounts of additional minerals that are characteristic of the geological region from which the sand derives. The presence of these minerals in the sand source will be reflected in the trace element content of a glass or faience object (Brems and Degryse, 2014; Henderson, 2012; Wedepohl et al., 2011).

Strontium commonly substitutes calcium in Ca-bearing minerals. Shells, composed of aragonite, have higher Sr values than calcite-rich limestones (Freestone et al., 2003; Wedepohl and Baumann, 2000), as Sr ions substitute Ca^{2+} more easily in the structure of aragonite (Mirti et al., 2008). As such, the CaO/Sr ratio has been used by many authors to distinguish between coastal sands with shell fragments and inland limestone-rich sands (e.g. Conte et al., 2018; Costa et al., 2021; Wedepohl et al., 2011). With the exception of sample CS4, the CaO/Sr values are generally below 200, with an average of 198 for the disk-shaped beads and 157 for sample C1, which is indicative of the use of coastal sands. On the other hand, the high CaO/Sr values of sample CS4, with an average value of 382, may indicate that this ratio is influenced by Ca-containing minerals other than carbonates (Conte et al., 2018). It is important to note that calcium phosphate was found in the core of sample CS4 (Fig. 4a and 4b), which can change the CaO/Sr values.

Zirconium and strontium contents have recently been used to distinguish Egyptian glass, from that produced in the Levant region (Costa et al., 2021; Truffa Giachet et al., 2019; Van Strydonck et al., 2018). In Fig. 13, the chondrite-normalized Sr and Zr values of the faience beads of Vinha das Caliças 4 are compared with those of the Phoenician-Punic glass beads from the same necropolis (Costa et al., 2021). As seen in Fig. 13, all faience beads of Vinha das Caliças 4 fall into the Levantine compositional window, even sample C1, the Egyptian blue frit bead. The extremely low Sr and Zr values of the disk-shaped faience beads, with average values of 40 ppm and 6 ppm, respectfully, may indicate that the sand used in their manufacture was carefully selected to increase raw material purity. In fact, calcite grains, limestone fragments and zircon grains were not identified in any of the 29 disk-shaped beads analyzed by VP-SEM-EDS. On the other hand, while the higher Sr

Table 3
LA-ICP-MS results of the line scans conducted on samples CS1, CS2, CS3 and CS4 (disk-shaped faience beads embedded in epoxy resin) and the Egyptian blue frit bead (sample C1) (Abbreviations: L.S. = line scan; Avg. = average; S.D. = standard deviation).

	CS1					CS2					CS3				
wt.%	L.S. 1	L.S. 2	L.S. 3	Avg.	S.D.	L.S. 1	L.S. 2	L.S. 3	Avg.	S.D.	L.S. 1	L.S. 2	L.S. 3	Avg.	S.D.
Al_2O_3	0.59	0.58	0.69	0.62	0.06	0.48	0.45	0.50	0.48	0.02	0.30	0.28	0.23	0.27	0.03
SiO_2	92.14	93.40	91.81	92.45	0.84	92.14	92.98	91.67	92.26	0.66	95.34	95.72	96.25	95.77	0.46
CaO	1.78	1.19	1.16	1.37	0.35	1.34	0.71	0.73	0.93	0.36	0.42	0.57	0.39	0.46	0.10
MnO	0.17	0.17	0.33	0.22	0.09	0.23	0.31	0.54	0.36	0.16	0.35	0.34	0.29	0.33	0.03
FeO	1.62	1.28	1.53	1.48	0.18	2.11	2.05	3.00	2.39	0.53	0.79	0.73	0.67	0.73	0.06
CuO	1.79	1.62	2.41	1.94	0.42	2.09	1.80	1.77	1.89	0.17	1.18	1.10	1.02	1.10	0.08
ppm															
Na	697.73	658.60	1454.37	936.90	448.57	649.72	573.02	679.51	634.08	54.94	1113.85	971.23	787.73	957.60	163.49
Mg	1264.38	830.54	1655.35	1250.09	412.59	871.14	917.63	1415.48	1068.08	301.75	398.33	332.00	266.20	332.18	66.07
K	497.26	503.36	1025.76	675.46	303.38	373.63	678.50	226.33	426.15	230.62	349.60	637.73	520.39	502.57	144.89
Sc	1.49	1.63	1.68	1.60	0.10	1.72	1.63	2.02	1.79	0.20	1.51	1.66	1.36	1.51	0.15
Ti	283.96	280.54	321.49	295.33	22.72	317.95	347.13	527.88	397.65	113.72	147.40	148.85	128.86	141.70	11.15
V	9.67	10.25	19.23	13.05	5.36	11.35	15.81	22.10	16.42	5.40	15.09	14.42	12.47	13.99	1.36
Cr	5.80	3.70	3.77	4.42	1.19	3.88	3.89	4.51	4.09	0.36	2.41	2.62	2.06	2.36	0.28
Co	328.01	189.91	290.71	269.54	71.44	210.41	211.44	453.38	291.74	139.98	234.77	228.93	246.29	236.66	8.83
Ni	97.14	86.84	160.19	114.72	39.71	144.74	146.31	147.50	146.18	1.38	82.15	95.76	78.78	85.56	8.99
Zn	78.52	89.10	145.99	104.54	36.29	99.36	94.77	97.11	97.08	2.30	86.45	75.84	75.90	79.40	6.11
As	40.88	29.38	63.07	44.44	17.13	32.37	47.10	63.95	47.81	15.80	65.52	62.33	53.03	60.29	6.49
Rb	3.67	4.72	6.04	4.81	1.19	3.82	3.22	3.10	3.38	0.39	2.86	2.99	1.62	2.49	0.75
Sr	42.92	59.97	101.81	68.23	30.30	58.45	44.39	46.68	49.84	7.54	34.62	28.84	20.90	28.12	6.89
Y	1.89	1.06	2.29	1.75	0.63	5.41	2.04	1.12	2.86	2.26	1.31	1.42	1.30	1.34	0.07
Zr	7.14	8.13	8.17	7.81	0.58	9.69	10.03	13.22	10.98	1.95	3.69	3.98	3.46	3.71	0.26
Nb	0.61	0.67	0.76	0.68	0.08	0.69	0.59	0.81	0.70	0.11	0.36	0.41	0.26	0.35	0.07
Sn	743.88	315.31	266.89	442.03	262.53	499.99	832.27	841.08	724.45	194.44	294.98	540.59	313.14	382.90	136.86
Sb	105.23	74.57	51.45	77.08	26.98	13.98	25.40	15.97	18.45	6.10	11.60	24.72	29.15	21.82	9.13
Cs	0.61	0.64	0.96	0.74	0.19	0.92	0.72	0.70	0.78	0.12	0.57	0.60	0.50	0.56	0.05
Ba	69.08	67.62	85.20	73.97	9.76	87.12	76.13	109.90	91.05	17.22	56.94	55.11	43.74	51.93	7.15

	CS1					CS2					CS3				
ppm	L.S. 1	L.S. 2	L.S. 3	Avg.	S.D.	L.S. 1	L.S. 2	L.S. 3	Avg.	S.D.	L.S. 1	L.S. 2	L.S. 3	Avg.	S.D.
La	2.14	1.04	2.22	1.80	0.66	4.69	1.67	1.18	2.51	1.90	1.23	1.26	1.03	1.17	0.12
Ce	4.45	2.61	4.55	3.87	1.09	3.92	2.80	7.94	4.89	2.70	2.80	3.21	2.44	2.82	0.39
Pr	0.58	0.28	0.55	0.47	0.17	1.18	0.45	0.31	0.65	0.47	0.31	0.34	0.25	0.30	0.05
Nd	2.47	1.12	2.40	2.00	0.76	5.13	1.84	1.32	2.76	2.07	1.22	1.40	1.09	1.24	0.16
Sm	0.57	0.26	0.53	0.45	0.17	1.29	0.49	0.30	0.70	0.52	0.28	0.31	0.26	0.28	0.02
Eu	0.16	0.08	0.19	0.14	0.06	0.33	0.12	0.18	0.21	0.11	0.14	0.10	0.08	0.11	0.03
Gd	0.47	0.22	0.48	0.39	0.15	1.14	0.40	0.26	0.60	0.47	0.25	0.29	0.25	0.26	0.02
Tb	0.07	0.05	0.08	0.07	0.01	0.19	0.08	0.05	0.11	0.07	0.04	0.06	0.04	0.05	0.01
Dy	0.40	0.24	0.46	0.37	0.12	1.11	0.37	0.24	0.57	0.47	0.23	0.27	0.21	0.23	0.03
Ho	0.09	0.05	0.10	0.08	0.02	0.21	0.08	0.06	0.12	0.08	0.06	0.08	0.06	0.06	0.01
Er	0.21	0.12	0.23	0.18	0.06	0.56	0.22	0.16	0.31	0.22	0.13	0.14	0.11	0.13	0.02
Tm	0.06	0.03	0.05	0.05	0.02	0.08	0.05	0.05	0.06	0.02	0.04	0.03	0.03	0.03	0.01
Yb	0.18	0.10	0.25	0.18	0.08	0.47	0.24	0.16	0.29	0.16	0.13	0.15	0.12	0.14	0.01
Lu	0.04	0.02	0.04	0.03	0.01	0.07	0.06	0.03	0.05	0.02	0.03	0.03	0.03	0.03	0.00
Hf	0.22	0.26	0.24	0.24	0.02	0.29	0.37	0.50	0.39	0.11	0.11	0.11	0.09	0.10	0.01
Ta	0.06	0.06	0.07	0.06	0.01	0.09	0.06	0.08	0.08	0.01	0.04	0.05	0.03	0.04	0.01
Pb	216.92	188.71	224.05	209.89	18.69	140.98	138.15	209.69	162.94	40.51	100.60	129.71	95.98	108.76	18.29
Bi	4.49	3.02	3.66	3.72	0.74	6.62	6.50	13.04	8.72	3.74	2.89	2.85	2.49	2.74	0.22
Th	0.31	0.31	0.47	0.36	0.09	0.59	0.42	0.31	0.44	0.14	0.17	0.22	0.12	0.17	0.05
U	0.14	0.13	0.20	0.16	0.04	0.11	0.27	0.12	0.17	0.09	0.11	0.16	0.09	0.12	0.03
ΣREE	11.89	6.22	12.11	10.07	3.34	20.38	8.86	12.25	13.83	5.92	6.90	7.65	5.99	6.84	0.83
CaO/Sr	414.35	197.98	113.59	241.97	155.13	229.31	160.97	156.39	182.22	40.84	122.00	198.34	187.50	169.28	41.30
Sn/Cu	0.05	0.02	0.01	0.03	0.02	0.03	0.06	0.06	0.05	0.01	0.03	0.06	0.04	0.04	0.01

	CS4					C1				
wt.%	L.S. 1	L.S. 2	L.S. 3	Avg.	S.D.	L.S. 1	L.S. 2	L.S. 3	Avg.	S.D.
Al_2O_3	0.16	0.26	0.28	0.23	0.06	1.18	1.05	1.08	1.10	0.07
SiO_2	95.96	95.37	94.75	95.36	0.60	71.99	77.34	77.64	75.66	3.18
CaO	0.81	0.96	1.19	0.99	0.19	8.53	7.79	6.60	7.64	0.97
MnO	0.17	0.20	0.22	0.20	0.03	<0.01	<0.01	<0.01	<0.01	<0.01
FeO	0.46	0.61	0.86	0.64	0.20	0.92	0.87	1.15	0.98	0.15
CuO	1.15	1.31	1.37	1.28	0.12	15.25	11.29	12.04	12.86	2.10
ppm										
Na	718.34	1039.83	1143.10	967.09	221.53	2712.76	3549.20	2644.50	2968.82	503.78
Mg	231.27	304.85	359.39	298.50	64.30	761.72	611.96	734.49	702.72	79.77
K	217.96	558.02	324.32	366.77	173.96	1057.58	1773.26	701.86	1177.57	545.68
Sc	1.35	1.83	1.88	1.69	0.29	2.22	1.81	2.21	2.08	0.23
Ti	92.32	137.67	145.85	125.28	28.84	897.83	898.56	1260.22	1018.87	209.02
V	8.34	10.87	11.39	10.20	1.63	7.05	6.68	9.05	7.59	1.28
Cr	13.93	1.74	1.93	5.87	6.98	9.08	9.74	13.22	10.68	2.22
Co	106.13	108.66	111.46	108.75	2.67	13.05	9.98	10.85	11.29	1.58
Ni	65.04	56.13	78.33	66.50	11.17	14.82	12.79	65.87	31.16	30.08

(*continued on next page*)

Table 3 (*continued*)

	CS4					C1				
wt.%	L.S. 1	L.S. 2	L.S. 3	Avg.	S.D.	L.S. 1	L.S. 2	L.S. 3	Avg.	S.D.
Zn	51.34	61.63	60.58	57.85	5.66	248.80	316.05	285.36	283.40	33.67
As	35.24	44.48	39.92	39.88	4.62	37.62	37.56	34.31	36.50	1.89
Rb	1.47	2.48	2.43	2.13	0.57	1.16	4.51	1.05	2.24	1.97
Sr	19.22	24.87	35.11	26.40	8.05	577.25	431.62	461.68	490.18	76.89
Y	1.55	2.61	2.55	2.24	0.60	3.63	4.13	2.61	3.46	0.77
Zr	2.45	6.41	3.70	4.19	2.02	45.96	46.03	46.45	46.15	0.27
Nb	0.26	0.36	0.37	0.33	0.06	2.06	2.20	2.60	2.29	0.28
Sn	1311.21	422.61	564.11	765.98	477.46	9030.13	3919.70	3944.85	5631.56	2943.27
Sb	17.06	20.96	20.76	19.59	2.20	101.78	104.12	168.01	124.64	37.58
Cs	0.43	0.41	0.51	0.45	0.05	0.06	0.05	0.08	0.07	0.01
Ba	47.03	52.64	60.44	53.37	6.73	139.04	112.06	114.13	121.74	15.02
	CS4					**C1**				
ppm	L.S. 1	L.S. 2	L.S. 3	Avg.	S.D.	L.S. 1	L.S. 2	L.S. 3	Avg.	S.D.
Na	718.34	1039.83	1143.10	967.09	221.53	2712.76	3549.20	2644.50	2968.82	503.78
Mg	231.27	304.85	359.39	298.50	64.30	761.72	611.96	734.49	702.72	79.77
K	217.96	558.02	324.32	366.77	173.96	1057.58	1773.26	701.86	1177.57	545.68
Sc	1.35	1.83	1.88	1.69	0.29	2.22	1.81	2.21	2.08	0.23
Ti	92.32	137.67	145.85	125.28	28.84	897.83	898.56	1260.22	1018.87	209.02
V	8.34	10.87	11.39	10.20	1.63	7.05	6.68	9.05	7.59	1.28
Cr	13.93	1.74	1.93	5.87	6.98	9.08	9.74	13.22	10.68	2.22
Co	106.13	108.66	111.46	108.75	2.67	13.05	9.98	10.85	11.29	1.58
Ni	65.04	56.13	78.33	66.50	11.17	14.82	12.79	65.87	31.16	30.08
Zn	51.34	61.63	60.58	57.85	5.66	248.80	316.05	285.36	283.40	33.67
As	35.24	44.48	39.92	39.88	4.62	37.62	37.56	34.31	36.50	1.89
Rb	1.47	2.48	2.43	2.13	0.57	1.16	4.51	1.05	2.24	1.97
Sr	19.22	24.87	35.11	26.40	8.05	577.25	431.62	461.68	490.18	76.89
Y	1.55	2.61	2.55	2.24	0.60	3.63	4.13	2.61	3.46	0.77
Zr	2.45	6.41	3.70	4.19	2.02	45.96	46.03	46.45	46.15	0.27
Nb	0.26	0.36	0.37	0.33	0.06	2.06	2.20	2.60	2.29	0.28
Sn	1311.21	422.61	564.11	765.98	477.46	9030.13	3919.70	3944.85	5631.56	2943.27
Sb	17.06	20.96	20.76	19.59	2.20	101.78	104.12	168.01	124.64	37.58
Cs	0.43	0.41	0.51	0.45	0.05	0.06	0.05	0.08	0.07	0.01
Ba	47.03	52.64	60.44	53.37	6.73	139.04	112.06	114.13	121.74	15.02
La	0.93	1.59	1.40	1.31	0.34	4.17	3.80	2.75	3.57	0.74
Ce	2.00	3.22	2.80	2.67	0.62	10.62	7.53	5.45	7.87	2.60
Pr	0.27	0.39	0.39	0.35	0.07	1.08	0.82	0.54	0.81	0.27
Nd	0.91	1.44	1.36	1.24	0.29	4.46	3.73	2.11	3.43	1.20
Sm	0.22	0.34	0.32	0.29	0.07	0.82	0.77	0.48	0.69	0.18
Eu	0.09	0.13	0.13	0.12	0.02	0.24	0.19	0.10	0.18	0.07
Gd	0.25	0.40	0.34	0.33	0.08	0.71	0.72	0.39	0.61	0.19
Tb	0.06	0.10	0.08	0.08	0.02	0.12	0.12	0.09	0.11	0.02
Dy	0.30	0.51	0.49	0.43	0.12	0.62	0.66	0.43	0.57	0.12
Ho	0.07	0.12	0.11	0.10	0.03	0.14	0.15	0.09	0.13	0.04
Er	0.16	0.27	0.25	0.22	0.06	0.40	0.38	0.27	0.35	0.07
Tm	0.03	0.05	0.04	0.04	0.01	0.05	0.06	0.04	0.05	0.01
Yb	0.15	0.23	0.24	0.21	0.05	0.35	0.37	0.31	0.34	0.03
Lu	0.03	0.04	0.04	0.04	0.01	0.05	0.06	0.04	0.05	0.01
Hf	0.09	0.20	0.13	0.14	0.05	1.15	1.19	1.19	1.18	0.02
Ta	0.04	0.04	0.03	0.04	0.00	0.19	0.21	0.25	0.21	0.03
Pb	101.90	123.31	182.75	135.99	41.89	628.24	731.75	580.35	646.78	77.38
Bi	3.42	4.52	4.15	4.03	0.56	460.38	441.66	584.89	495.64	77.85
Th	0.12	0.46	0.14	0.24	0.19	0.78	0.85	0.89	0.84	0.06
U	0.09	0.13	0.12	0.11	0.02	0.25	0.27	0.30	0.27	0.03
ΣREE	5.44	8.84	7.99	7.42	1.77	23.83	19.35	13.08	18.76	5.40
CaO/Sr	420.21	387.72	339.21	382.38	40.76	147.76	180.55	143.06	157.12	20.42
Sn/Cu	0.14	0.04	0.05	0.08	0.05	0.07	0.04	0.04	0.05	0.02

values of sample C1 (with an average value of 490 ppm) are consistent with the use of coastal sands, it is important to note that these values may be influenced by the presence of the synthetic Egyptian blue pigment used to impart its characteristic hue to the bead.

An overview of chondrite-normalized trace elements (Fig. 14) highlights the similarities between the disk-shaped beads analyzed, and the difference between these faience beads and sample C1. In fact, sample C1 is enriched in Ti, Sr, Zr, Nb, Hf, Ta and Th, when compared to the disk-shaped beads. Titanium is frequently associated with iron, and as such can be found in Fe and/or Ti oxides, while Hf commonly substitutes Zr in the structure of zircon ($ZrSiO_4$), a very resistant and stable mineral found in sands used for glass and glaze production (Brems and Degryse, 2014; Henderson, 2012; Wedepohl et al., 2011). Tantalum and niobium, on the other hand, generally occur in association, in minerals such as those that form the columbite-tantalite series (Albrecht et al., 2011b, 2011a). These minerals, as well as Th-bearing minerals, occur in granitic and pegmatitic rocks, as well as secondary placer deposits (Albrecht et al., 2011b, 2011a; Stoll, 2000). These results are consistent with the use of a sand with significant heavy mineral contents in the manufacture of the Egyptian blue frit bead or the Egyptian blue pigment.

The results of the line scan analysis also enabled the determination of Sn/Cu ratios, which have been used as an indicator of the use of bronze as a faience colorant (Tite and Shortland, 2008). As seen in Table 3, the Sn/Cu ratios range between 0.03 and 0.08 in the disk-shaped beads CS1 to CS4, which may indicate that 3–8 % tin bronze scrapings were used in the production of these adornment objects.

Disk-shaped faience beads, similar to those recovered from the necropolis of Vinha das Caliças 4, have been found in many contexts

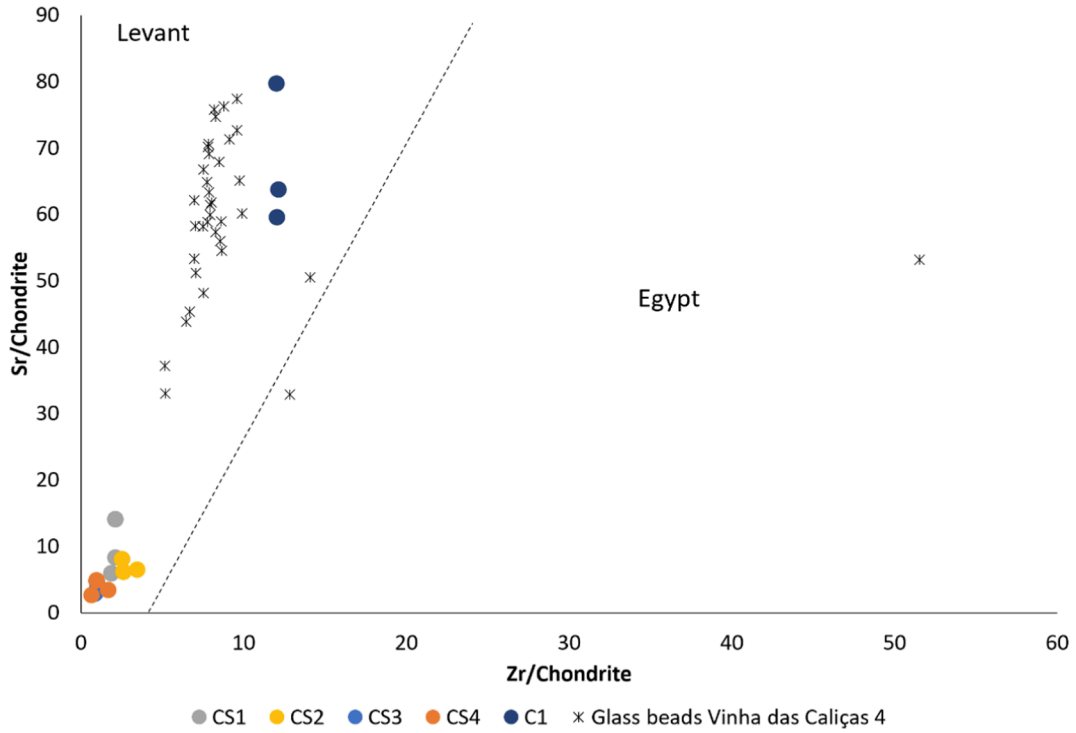

Fig. 13. Chondrite-normalized (McDonough and Sun, 1995) Sr and Zr values of the faience beads of Vinha das Caliças 4, as well as the glass beads from the same necropolis (Costa et al., 2021). All faience beads, including the Egyptian blue frit bead, seem to have been manufactured in the Levant region. (For interpretation of the references to color in this figure legend, the reader is referred to the web version of this article.)

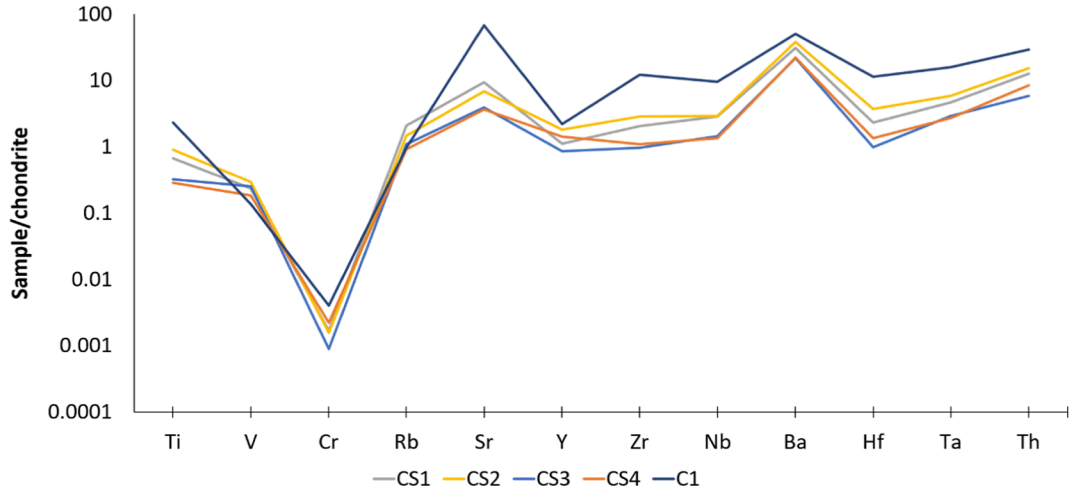

Fig. 14. Chondrite-normalized (McDonough and Sun, 1995) trace element composition of the faience beads of Vinha das Caliças 4. While the disk-shaped beads (CS1-CS4) have similar compositions, sample C1, the cubic-shaped Egyptian blue frit bead, is enriched in Ti, Sr, Zr, Nb. Hf, Ta and Th, when compared to the remaining beads analyzed. Average values for each sample are represented. (For interpretation of the references to color in this figure legend, the reader is referred to the web version of this article.)

throughout Egypt, Levant and Cyprus and within the spoils of the Uluburun shipwreck (Ingram, 2005). In Southern Portugal, these beads have been found in Iron Age burials and necropolis dated between the 8th and the 6th century BCE (Arruda et al., 2016; Dias et al., 1970; Monge-Soares et al., 2016; Santos et al., 2009), but are commonly misidentified and labeled as vitreous paste or ceramic beads (Monge-Soares et al., 2016), and have yet to be studied from an archaeometric perspective. However, other Egyptian blue frit beads are yet to be uncovered in Southern Portugal. Nevertheless, the presence of these faience beads, as well as the Egyptian blue frit bead, in inland Southwestern Iberian contexts, can be considered to be a testament of long-distance trading between the region and Eastern Mediterranean civilizations.

4. Conclusions

A collection of 30 faience beads recovered from the Iron Age necropolis of Vinha das Caliças 4 (Beja, Portugal), was analyzed in order to identify their production technology and provide insights into their possible provenance. The multi-analytical approach employed, combining laser ablation inductively coupled plasma mass spectrometry (LA-ICP-MS), variable pressure scanning electron microscope coupled

with energy dispersive X-ray spectrometry (VP-SEM-EDS) and micro-X-ray diffraction (μ-XRD), called attention to the difficulties that arise from the analysis of weathered faience objects and that are augmented by their intrinsic heterogeneous nature.

VP-SEM-EDS analysis and LA-ICP-MS mapping revealed that the disk-shaped faience beads were manufactured using the cementation glazing method. Weathering precluded the undisputed identification of the fluxing agent used in the manufacture of these faience beads. However, the low MgO values, combined with the significant Cl concentrations, could indicate that natron was used in their production. The high degree of weathering of the faience beads also precluded their LA-ICP-MS analysis using a spot analysis sampling strategy and raised an important issue regarding the use of minimally invasive analyses to determine the provenance of weathered faience objects.

Copper, most likely in the form of bronze scrapings, was used to impart a blue-green hue to the disk-shaped beads. The cubic-shaped bead, on the other hand, identified by VP-SEM-EDS and μ-XRD as an Egyptian blue frit, owes its vivid blue color to the tabular crystals of this well-known synthetic pigment.

Trace element analysis suggests that all beads were manufactured in the Levant region using coastal sands. Micro-XRD and LA-ICP-MS revealed that the disk-shaped beads were manufactured using feldspathic sand with low amounts of carbonates and zircon, which may have been carefully selected to increase raw material purity. However, these sands contained iron oxides, as attested by the presence of iron-rich grains within the core and interaction layers of the disk-shaped faience beads. Conversely, the cubic Egyptian blue frit bead was produced using sand with significant heavy mineral contents, likely from a placer deposit. While these results may indicate that the two types of faience beads found in Vinha das Caliças 4 were produced in different workshops, using raw material sources from distinct geological provinces, or alternatively, different raw material treatment methods, the influence of the Egyptian blue pigment on trace element analysis is not known and should be explored in future studies. These results also confirm the existence of long-distance trading between the Eastern Mediterranean and Southwestern Iberia in the 1st millennium B.C.

Ultimately, this study highlighted the importance of the use of a combination of microstructural and geochemical criteria in the identification of faience production technology and provenance. The importance of the selection of the sampling strategy in LA-ICP-MS analysis of faience objects was also emphasized.

CRediT authorship contribution statement

Mafalda Costa: Conceptualization, Methodology, Validation, Formal analysis, Investigation, Visualization, Funding acquisition, Project administration, Writing - original draft. **Pedro Barrulas:** Conceptualization, Methodology, Validation, Formal analysis, Investigation, Writing - review & editing. **Ana Margarida Arruda:** Conceptualization, Resources, Writing - review & editing. **Rui Barbosa:** Conceptualization, Resources. **Peter Vandenabeele:** Conceptualization, Funding acquisition, Writing - review & editing. **José Mirão:** Conceptualization, Resources, Investigation, Funding acquisition, Writing - review & editing.

Declaration of Competing Interest

The authors declare that they have no known competing financial interests or personal relationships that could have appeared to influence the work reported in this paper.

Data availability

Data will be made available on request.

Acknowledgements

This work has been financially supported by the UIDB/04449/2020 and UIDP/04449/2020 projects, as well as the PP-nGLASS – An interdisciplinary study of the impact of the Phoenician-Punic natron glass trade in Iberian communities – project (EXPL/HAR-ARQ/0381/2021), which were funded by Fundação para a Ciência e Tecnologia (FCT) and by the European Regional Development Fund. M. Costa also acknowledges FCT for a Ph.D. Fellowship (SFRH/BD/128889/2017) co-funded by the European Social Fund and by Portuguese national funds. The financial support of a Concerted Research Action of Ghent University (B/13340/02) is also acknowledged.

The authors would also like to thank ArqueoHoje for providing access to the archaeological artifacts.

The authors would also like acknowledge the anonymous reviewers that, due to their insightful comments and suggestions, greatly improved the quality of this manuscript.

Appendix A. Supplementary data

Supplementary data to this article can be found online at https://doi.org/10.1016/j.jasrep.2022.103703.

References

Abdel-Karim, A.A.M., El-Shafey, A.H.M., 2012. Mineralogy and chemical distribution study of placer cassiterite and some associated new recorded minerals, east rosetta, egypt. Arabian Journal of Geosciences 5, 807–816. https://doi.org/10.1007/s12517-011-0282-y.

Albrecht, S., Cymorek, C., Andersson, K., Reichert, K., Wolf, R., 2011a. Tantalum and Tantalum Compounds. Ullmann's Encyclopedia of Industrial Chemistry. https://doi.org/10.1002/14356007.a26_071.pub2.

Albrecht, S., Cymorek, C., Eckert, J., 2011b. Niobium and Niobium Compounds. Ullmann's Encyclopedia of Industrial Chemistry. https://doi.org/10.1002/14356007.a17_251.pub2.

Angelini, I., Artioli, G., Bellintani, P., Diella, V., Gemmi, M., Polla, A., Rossi, A., 2004. Chemical analyses of Bronze Age glasses from Frattesina di Rovigo, Northern Italy. Journal of Archaeological Science 31, 1175–1184. https://doi.org/10.1016/j.jas.2004.02.015.

Arruda, A.M., Barbosa, R., Gomes, F., de Sousa, E., 2016. A Necrópole de Vinha das Caliças (Beja, Portugal). In: Jiménez Ávila, J. (Ed.), Sidereum Ana III - El Río GuadiAna Y Tartessos. Consórcio de la Ciudad Monumental Histórico-Artística y Arqueológica de Mérida, Mérida, pp. 187–225.

Bliem, R., Pavelec, J., Gamba, O., McDermott, E., Wang, Z., Gerhold, S., Wagner, M., Osiecki, J., Schulte, K., Schmid, M., Blaha, P., Diebold, U., Parkinson, G.S., 2015. Adsorption and incorporation of transition metals at the magnetite Fe3 O4 (001) surface. Physical Review B - Condensed Matter and Materials Physics 92, 1–9. https://doi.org/10.1103/PhysRevB.92.075440.

Brems, D., Degryse, P., 2014. Trace element analysis in provenancing Roman glassmaking. Archaeometry 56, 116–136. https://doi.org/10.1111/arcm.12063.

Conte, S., Arletti, R., Henderson, J., Degryse, P., Blomme, A., 2018. Different glassmaking technologies in the production of Iron Age black glass from Italy and Slovakia. Archaeological and Anthropological Sciences 10, 503–521. https://doi.org/10.1007/s12520-016-0366-4.

Costa, M., Arruda, A.M., Barbosa, R., Barrulas, P., Vandenabeele, P., Mirão, J., 2019a. A Micro-Analytical Study of the Scarabs of the Necropolis of Vinha das Caliças (Portugal). Microscopy and Microanalysis 25, 214–220. https://doi.org/10.1017/S143192761801560X.

Costa, M., Arruda, A.M., Dias, L., Barbosa, R., Mirão, J., Vandenabeele, P., 2019b. The combined use of Raman and micro-X-ray diffraction analysis in the study of archaeological glass beads. Journal of Raman Spectroscopy 50, 250–261. https://doi.org/10.1002/jrs.5446.

Costa, M., Barrulas, P., Arruda, A.M., Dias, L., Barbosa, R., Vandenabeele, P., Mirão, J., 2021. An insight into the provenance of the Phoenician-Punic glass beads of the necropolis of Vinha das Caliças (Beja, Portugal). Archaeological and Anthropological Sciences 13, 149. https://doi.org/10.1007/s12520-021-01390-5.

Costa, M., Barrulas, P., Dias, L., da Conceição Lopes, M., Barreira, J., Clist, B., Karklins, K., da Piedade de Jesus, M., da Silva Domingos, S., Vandenabeele, P., Mirão, J., 2019c. Multi-analytical approach to the study of the European glass beads found in the tombs of Kulumbimbi (Mbanza Kongo, Angola). Microchemical Journal 149, 103990. https://doi.org/10.1016/j.microc.2019.103990.

Costa, M., Barrulas, P., Dias, L., Lopes, M. da C., Barreira, J., Clist, B., Karklins, K., de Jesus, M. da P., da Silva Domingos, S., Moens, L., Vandenabeele, P., Mirão, J., 2020. Determining the provenance of the European glass beads of Lumbu (Mbanza Kongo, Angola). Microchemical Journal 154, 104531. https://doi.org/10.1016/j.microc.2019.104531.

Costa, R.C.C., Lelis, M.F.F., Oliveira, L.C.A., Fabris, J.D., Ardisson, J.D., Rios, R.R.V.A., Silva, C.N., Lago, R.M., 2006. Novel active heterogeneous Fenton system based on

Fe3-xM xO4 (Fe Co, Mn, Ni): The role of M2+ species on the reactivity towards H2O2 reactions. Journal of Hazardous Materials 129, 171–178. https://doi.org/10.1016/j.jhazmat.2005.08.028.
D'Oriano, C., Dapelo, S., Podda, F., Cioni, R., 2008. Laser-ablation inductively coupled plasma mass spectrometry (LA-ICP-MS): Setting operating conditions and instrumental performance. Periodico di Mineralogia 77, 65–74. https://doi.org/10.2451/2008PM0019.
Dias, M.M.A., Beirão, C. de M., Coelho, L., 1970. Duas necrópoles da Idade do Ferro no Baixo Alentejo: Ourique. O Arqueólogo Português 3, 175–219.
Dussubieux, L., Robertshaw, P., Glascock, M.D., 2009. LA-ICP-MS analysis of African glass beads: Laboratory inter-comparison with an emphasis on the impact of corrosion on data interpretation. International Journal of Mass Spectrometry 284, 152–161. https://doi.org/10.1016/j.ijms.2008.11.003.
Freestone, I.C., Ponting, M., Hughes, M.J., 2002. The Origins of Byzantine Glass from Maroni Petrea, Cyprus. Archaeometry 44, 257–272.
Freestone, I.C., Leslie, K.A., Thirlwall, M., Gorin-Rosen, Y., 2003. Strontium Isotopes in the Investigation of Early Glass Production: Byzantine and Early Islamic Glass from the Near East. Archaeometry 45, 19–32. https://doi.org/10.1111/1475-4754.00094.
Graf, G.G., 2000. Tin, Tin Alloys, and Tin Compounds. Ullmann's Encyclopedia of Industrial Chemistry. https://doi.org/10.1002/14356007.a27_049.
Grifa, C., Cavassa, L., De Bonis, A., Germinario, C., Guarino, V., Izzo, F., Kakoulli, I., Langella, A., Mercurio, M., Morra, V., Lloyd, I., 2016. Beyond Vitruvius: New Insight in the Technology of Egyptian Blue and Green Frits. Journal of the American Ceramic Society 99 (10), 3467–3475.
Griffiths, D., 2006. Analysis of Egyptian Faience Vessel Fragments Excavated in Sidon in 2005. Archaeology & History in the Lebanon 129–137.
Gu, Z., Zhu, J., Xie, Y., Xiao, T., Yang, Y., Wang, C., 2014. Nondestructive analysis of faience beads from the Western Zhou Dynasty, excavated from Peng State cemetery, Shanxi Province, China. Journal of Analytical Atomic Spectrometry 29, 1438–1443. https://doi.org/10.1039/c4ja00031e.
Gu, Z., Kenoyer, J.M., Yang, Y., 2016. Investigation of ancient Harappan faience through LA-ICP-AES and SR-μCT. Journal of Instrumentation 11 (04), C04001–C.
Hatton, G.D., Shortland, A.J., Tite, M.S., 2008. The production technology of Egyptian blue and green frits from second millennium BC Egypt and Mesopotamia. Journal of Archaeological Science 35, 1591–1604. https://doi.org/10.1016/j.jas.2007.11.008.
Hellemans, K., Cagno, S., Bogana, L., Janssens, K., Mendera, M., 2019. LA-ICP-MS labels early medieval Tuscan finds from Siena and Donoratico as late natron glass. Journal of Archaeological Science: Reports 23, 844–853. https://doi.org/10.1016/j.jasrep.2018.12.002.
Henderson, J., 2012. The Provenance of Ancient Man-made Glass: Raw Materials and the Use of Chemical and Isotopic Analytical Techniques. In: Liritzis, I., Stevenson, C.M. (Eds.), Obsidian and Ancient Manufactured Glasses. University of New Mexico Press, pp. 185–201.
Ingo, G.M., de Caro, T., Riccucci, C., Angelini, E., Grassini, S., Balbi, S., Bernardini, P., Salvi, D., Bousselmi, L., Çilingiroğlu, A., Gener, M., Gouda, V.K., Jarrah, O.A.L., Khosroff, S., Mahdjoub, Z., Saad, Z.A.L., El-Saddik, W., Vassiliou, P., 2006. Large scale investigation of chemical composition, structure and corrosion mechanism of bronze archeological artefacts from Mediterranean basin. Applied Physics A: Materials Science and Processing 83, 513–520. https://doi.org/10.1007/s00339-006-3550-z.
Ingram, R.S., 2005. Faience and Glass Beads from the Late Bronze Age Shipwreck at Uluburun. Texas A&M University.
Leslie, K.A., Freestone, I.C., Lowry, D., Thirlwall, M., 2006. The provenance and technology of Near Eastern glass: Oxygen isotopes by laser fluorination as a complement to strontium. Archaeometry 48, 253–270. https://doi.org/10.1111/j.1475-4754.2006.00255.x.
Mangone, A., De Benedetto, G.E., Fico, D., Giannossa, L.C., Laviano, R., Sabbatini, L., Van Der Werf, I.D., Traini, A., 2011. A multianalytical study of archaeological faience from the Vesuvian area as a valid tool to investigate provenance and technological features. New Journal of Chemistry 35, 2860–2868. https://doi.org/10.1039/c1nj20626e.
Matin, M., Matin, M., 2012. Egyptian faience glazing by the cementation method part 1: an investigation of the glazing powder composition and glazing mechanism. Journal of Archaeological Science 39, 763–776. https://doi.org/10.1016/j.jas.2011.11.013.
McDonough, W.F., Sun, S. -s., 1995. The composition of the Earth. Chemical Geology 120, 223–253. https://doi.org/10.1016/0009-2541(94)00140-4.
Mirti, P., Pace, M., Negro Ponzi, M.M., Aceto, M., 2008. ICP-MS analysis of glass fragments of Parthian and Sasanian epoch from Seleucia and Veh Ardašīr (Central Iraq). Archaeometry 50, 429–450. https://doi.org/10.1111/j.1475-4754.2007.00344.x.
Monge-Soares, R., Baptista, L., Rodrigues, Z., 2016. Os primeiros enterramentos sidéricos conhecidos na margem esquerda do Guadiana em território português. Revista Portuguesa de Arqueología 19, 129–141.
Musić, S., Ristic, M., 1992. Adsorption of zinc(II) on hydrous iron oxides. Journal of Radioanalytical and Nuclear Chemistry Articles 162, 351–362. https://doi.org/10.1007/BF02035395.
Nobel, J.V., 1969. The Technique of Egyptian Faience. American Journal of Archaeology 73, 435–439.
Oikonomou, A., Henderson, J., Gnade, M., Chenery, S., Zacharias, N., 2018. An archaeometric study of Hellenistic glass vessels: evidence for multiple sources. Archaeological and Anthropological Sciences 10 (1), 97–110.
Paynter, S., Jackson, C.M., 2022. Investigating Late Bronze Age Glass Beads from Stotfold, Bedfordshire, UK. Heritage 5, 634–645. https://doi.org/10.3390/heritage5020035.
Pearce, N.J.G., Perkins, W.T., Westgate, J.A., Gorton, M.P., Jackson, S.E., Neal, C.R., Chenery, S.P., 1997. A Compilation of New and Published Major and Trace Element Data for NIST SRM 610 and NIST SRM 612 Glass Reference Materials. Geostandards Newsletter – The Journal of Geostandards and Geoanalysis 21, 115–144. https://doi.org/10.1111/j.1751-908X.1997.tb00538.x.
Purowski, T., 2020. New Data on the Technology of Faience Production in Central Europe in the Early Bronze Age. Archaeometry 62, 563–576. https://doi.org/10.1111/arcm.12543.
Purowski, T., Syta, O., Wagner, B., 2019. Mycenaean and Egyptian faience beads discovered in southern Poland. Journal of Archaeological Science: Reports 28, 102023. https://doi.org/10.1016/j.jasrep.2019.102023.
Ragab, H., Khalil, M., Yousry, A., El Afandy, A., 2017. Inferred Resources and Environmental Impact of the Top Meter Black Sands in the Coastal Area of Mediterranean Sea Between Damietta Sea Port and Gamasa City. Egypt. Al-Azhar Bulletin of Science 28, 1–13. https://doi.org/10.21608/absb.2017.8169.
Rehren, T., 2008. A review of factors affecting the composition of early Egyptian glasses and faience: alkali and alkali earth oxides. Journal of Archaeological Science 35, 1345–1354. https://doi.org/10.1016/j.jas.2007.09.005.
Riederer, J., 1997. Egyptian Blue. In: Fitzhugh, E.W. (Ed.), Artists' Pigments. National Gallery of Art and Archetype Publications Ltd., London, pp. 23–46.
Robinet, L., Eremin, K., 2012. Glass, in: Edwards, H., Vandenabeele, P. (Eds.), Analytical Archaeometry: Selected Topics. RSC Publishing, Cambridge, UK, pp. 268–290. https://doi.org/10.1039/9781849732741.
Saitowitz, S.J., 1996. Glass Beads as Indicators of Contact and Trade in Southern Africa ca. University of Cape Town.
Santopadre, P., Verità, M., 2000. Analyses of the Production Technologies of Italian Vitreous Materials of the Bronze Age. Journal of Glass Studies 42, 25–40.
Santos, F.J.C., Tamissa Antunes, A.S., Grilo, C., Deus, M. de, 2009. A necrópole da I Idade do Ferro de Palhais (Beringel, Beja). Resultados preliminares de uma intervenção de emergência no Baixo-Alentejo, in: IV Encuentro de Arqueología Del Suroeste Peninsular. pp. 746–804.
Shortland, A.J., 2002. The use and origin of antimonate colorants in early Egyptian glass. Archaeometry 44, 517–530. https://doi.org/10.1111/1475-4754.t01-1-00083.
Shortland, A.J., Schachner, L., Freestone, I., Tite, M., 2006. Natron as a flux in the early vitreous materials industry: Sources, beginnings and reasons for decline. Journal of Archaeological Science 33, 521–530. https://doi.org/10.1016/j.jas.2005.09.011.
Shortland, A.J., Rogers, N., Eremin, K., 2007b. Trace element discriminants between Egyptian and Mesopotamian Late Bronze Age glasses. Journal of Archaeological Science 34, 781–789. https://doi.org/10.1016/j.jas.2006.08.004.
Shortland, A., Shishlina, N., Egorkov, A., 2007a. Origin and Production of Faience Beads in the North Caucasus and the Northwest Caspian Sea Region in the Bronze Age. In: Lyonnet, B. (Ed.), Les Cultures Du Caucase (VIe-IIIe Millénaires Avant Notre Ère). Leurs Relations Avec Le Proche-Orient, CNRS Éditions, pp. 269–283.
Smirniou, M., Rehren, T., 2013. Shades of blue - cobalt-copper coloured blue glass from New Kingdom Egypt and the Mycenaean world: A matter of production or colourant source? Journal of Archaeological Science 40, 4731–4743. https://doi.org/10.1016/j.jas.2013.06.029.
Stoll, W., 2000. Thorium and Thorium Compounds. Ullmann's Encyclopedia of Industrial Chemistry. https://doi.org/10.1002/14356007.a27_001.
Tite, M.S., Shortland, A.J., 2008. Production Technology of Faience and Related Early Vitreous Materials.
Tite, M.S., Bimson, M., 1986. Faience: An Investigation of the Microstructures Associated with the Different Methods of Glazing. Archaeometry 28, 69–78. https://doi.org/10.1111/j.1475-4754.1986.tb00375.x.
Tite, M.S., Freestone, I.C., Bimson, M., 1983. Egyptian Faience: an Investigation of the Methods of Production. Archaeometry 25, 17–27. https://doi.org/10.1111/j.1475-4754.1983.tb00658.x.
Tite, M.S., Manti, P., Shortland, A.J., 2007. A technological study of ancient faience from Egypt. Journal of Archaeological Science 34, 1568–1583. https://doi.org/10.1016/j.jas.2006.11.010.
Tite, M.S., Maniatis, Y., Kavoussanaki, D., Panagiotaki, M., Shortland, A.J., Kirk, S.F., 2009. Colour in Minoan faience. Journal of Archaeological Science 36 (2), 370–378.
Toffolo, M.B., Klein, E., Elbaum, R., Aja, A.J., Master, D.M., Boaretto, E., 2013. An early Iron Age assemblage of faience beads from Ashkelon, Israel: Chemical composition and manufacturing process. Journal of Archaeological Science 40, 3626–3635. https://doi.org/10.1016/j.jas.2013.05.010.
Truffa Giachet, M., Gratuze, B., Ozainne, S., Mayor, A., Huysecom, E., 2019. A Phoenician glass eye bead from 7th–5th c. cal BCE Nin-Bèrè 3, Mali: Compositional characterisation by LA–ICP–MS. Journal of Archaeological Science: Reports 24, 748–758. https://doi.org/10.1016/j.jasrep.2019.02.032.
van Elteren, J.T., Tennent, N.H., Šelih, V.S., 2009. Multi-element quantification of ancient/historic glasses by laser ablation inductively coupled plasma mass spectrometry using sum normalization calibration. Analytica Chimica Acta 644, 1–9. https://doi.org/10.1016/j.aca.2009.04.025.
Van Strydonck, M., Gratuze, B., Rolland, J., De Mulder, G., 2018. An archaeometric study of some pre-Roman glass beads from Son Mas (Mallorca, Spain). Journal of Archaeological Science: Reports 17, 491–499. https://doi.org/10.1016/j.jasrep.2017.12.003.
Vandiver, P.B., 1998. A review and proposal of new criteria for production technologies of Egyptian faience. In: Colinart, S., Menu, M. (Eds.), La Couleur Dans La Peinture et l'émaillage de l'Egypte Ancienne. Edipuglia, Bari, pp. 121–139.

Wedepohl, K.H., Baumann, A., 2000. The use of marine molluskan shells for Roman glass and local raw glass production in the Eifel area (western Germany). Naturwissenschaften 87, 129–132. https://doi.org/10.1007/s001140050690.

Wedepohl, K.H., Simon, K., Kronz, A., 2011. Data on 61 chemical elements for the characterization of three major glass compositions in Late Antiquity and the Middle Ages. Archaeometry 53, 81–102. https://doi.org/10.1111/j.1475-4754.2010.00536.x.

Zhong, Y., Liang, X., Tan, W., Zhong, Y., He, H., Zhu, J., Yuan, P., Jiang, Z., 2013. A comparative study about the effects of isomorphous substitution of transition metals (Ti, Cr, Mn, Co and Ni) on the UV/Fenton catalytic activity of magnetite. Journal of Molecular Catalysis A: Chemical 372, 29–34. https://doi.org/10.1016/j.molcata.2013.01.038.